

Accepted for publication in the Astrophysical Journal

Oxygen and Nitrogen in Isolated Dwarf Irregular Galaxies

Liese van Zee

Astronomy Department, Indiana University, 727 E 3rd St, Bloomington, IN 47405

`vanzee@astro.indiana.edu`

and

Martha P. Haynes

*Center for Radiophysics and Space Research and National Astronomy and Ionosphere Center,¹
Cornell University, Ithaca, NY 14853*

`haynes@astro.cornell.edu`

ABSTRACT

We present long slit optical spectroscopy of 67 H II regions in 21 dwarf irregular galaxies to investigate the enrichment of oxygen, nitrogen, neon, sulfur, and argon in low mass galaxies. Oxygen abundances are obtained via direct detection of the temperature sensitive emission lines for 25 H II regions; for the remainder of the sample, oxygen abundances are estimated from strong line calibrations. The direct abundance determinations are compared to the strong-line abundance calibrations of both McGaugh (1991) and Pilyugin (2000). While the McGaugh (1991) calibration yields a statistical offset of 0.07 dex, the photoionization model grid traces the appropriate iso-metallicity contour shape in the R23-O32 diagnostic diagram. In contrast, while the Pilyugin (2000) calibration yields a negligible statistical offset, the residuals in this strong-line calibration method are correlated with ionization parameter. Thus, these observations indicate that oxygen abundances will be overestimated by the p-method for H II regions with low ionization parameters. Global oxygen and nitrogen abundances for this sample of dwarf irregular galaxies are examined in the context of open and closed box chemical evolution models. While several galaxies are consistent with closed box chemical evolution, the majority of this sample have an effective yield $\sim 1/4$ of the expected yield for a constant star formation rate and Salpeter IMF, indicating that either outflow of enriched gas or inflow of pristine gas has occurred. The effective yield strongly correlates

¹The National Astronomy and Ionosphere Center is operated by Cornell University under a cooperative agreement with the National Science Foundation.

with M_H/L_B in the sense that gas-rich galaxies are more likely to be closed systems. However, the effective yield does not appear to correlate with other global parameters such as dynamical mass, absolute magnitude, star formation rate or surface brightness. In addition, open and closed systems are not identified easily in other global abundance measures; for example, the observed correlation between luminosity and metallicity is consistent with other recent results in the literature. A correlation is found between the observed nitrogen-to-oxygen ratio and the color of the underlying stellar population; redder dwarf irregular galaxies have higher N/O ratios than blue dwarf irregular galaxies. The relative abundance ratios are interpreted in the context of delayed release of nitrogen and varied star formation histories.

Subject headings: galaxies: abundances — galaxies: dwarf — galaxies: evolution — galaxies: irregular

1. Introduction

Gas phase oxygen and nitrogen abundances are two of the most robust measures of the intrinsic metallicity of gas-rich low mass galaxies. Over the last three decades, numerous studies have measured the oxygen and nitrogen abundances of H II regions in dwarf irregular galaxies (e.g., Alloin et al. 1979; Lequeux et al. 1979; Kinman & Davidson 1981; Campbell, Terlevich, & Melnick 1986; Garnett 1990; Miller & Hodge 1996; van Zee et al. 1997a; Izotov & Thuan 1998; Hidalgo-Gómez & Olofsson 2002; Skillman, Côté, & Miller 2003; Lee, Grebel, & Hodge 2003; Lee, Salzer, & Melbourne 2004). Lequeux et al. (1979) were the first to note a strong correlation between metallicity and mass, in the sense that more massive galaxies also have higher measured oxygen abundances (see also Kinman & Davidson 1981); Skillman et al. (1989) determined that a stronger correlation was found between metallicity and luminosity (see also Richer & McCall 1995; Hunter & Hoffman 1999; Pilyugin 2001; Tremonti et al. 2004, for an alternative view, see Hidalgo-Gómez & Olofsson 1998). However, despite extensive observational effort, the origin of the luminosity-metallicity relation is still poorly understood. One possibility is that it represents an evolutionary sequence, in which more luminous galaxies have processed a larger fraction of their raw materials. Alternatively, it may represent a mass retention sequence, in which more luminous (massive) galaxies are able to retain a larger fraction of their processed materials. In the former case, one would expect to see a stronger correlation between gas-mass fraction and metallicity; in the latter case, one would expect to see a difference between the metallicity-luminosity relation traced by elements formed in highly energetic Type II SN (such as oxygen) and in the relation traced by elements formed in lower mass stars (such as nitrogen). Clearly, one key to understanding the metallicity-luminosity relation is to look for additional parameters which are responsible for the scatter in the correlation. With this goal in mind, we present oxygen and nitrogen abundances in 67 H II regions in 21 well-studied dwarf irregular galaxies which span a moderate range in luminosity.

Of particular interest is whether there are significant second parameter effects in the global abundance trends due to variations of surface brightness, color, gas mass fraction, average star formation rate, or other evolutionary effects (see, e.g., Garnett 2002; Kobulnicky et al. 2003; Tremonti et al. 2004). The galaxies in this study are part of an extensive optical imaging program of isolated dwarf irregular galaxies and thus a substantial amount of supporting data exists in the literature (van Zee et al. 1997a; van Zee 2000b). This sample includes galaxies with a wide range of surface brightness ($20 < \mu_B^0 < 26$ mag arcsec $^{-2}$), gas mass fraction ($0.4 < f_{\text{gas}} < 0.95$), and current star formation rate ($0.002 < SFR < 0.16$ M $_{\odot}$ yr $^{-1}$), but only a modest range of color (B-V $\sim 0.4 \pm 0.1$). Most of the galaxies in this sample are relatively isolated (d > 200 kpc to nearest neighbor), and thus have not had significant alterations of their star formation activity or elemental enrichment due to tidal interactions within the last few Gyr. Thus, elemental abundance measurements of this well-studied sample of galaxies will provide insight into the chemical evolution and enrichment processes of low mass galaxies.

This paper presents the results of long-slit optical spectroscopy of 21 dwarf irregular galaxies. The observations and data reduction procedures are discussed in Section 2. Derivation of nebular abundances via direct and strong line methods are described in Section 3. Correlations between both oxygen and nitrogen abundances and other global parameters are discussed in the context of open and closed box chemical evolution models in Section 4. Section 5 contains a brief summary of the conclusions.

2. Observations

2.1. Sample Selection

The dwarf irregular galaxies for the present study were selected from the optical imaging sample of van Zee (2000b, 2001). This sample of dwarf irregular galaxies was selected primarily from the *Uppsala General Catalog of Galaxies* (Nilson 1973, UGC) based on morphological classification, apparent diameter ($D < 7'$), gas-richness ($\int Sdv/W > 50$ mJy), and apparent isolation (no known neighbor within $30'$ and 500 km s $^{-1}$). The present sample contains galaxies classified as late-type spiral or irregular, with $M_B > -18.0$, and with heliocentric velocities less than 2000 km s $^{-1}$. Basic parameters for the selected galaxies are tabulated in Table 1.

Table 1 includes a distance estimate adopted from the literature for those galaxies with TRGB observations [UGC 685 (Maíz-Apellániz et al. 2002), HKK97 L14 (Karachentsev et al. 2004), UGC 4483 (Dolphin et al. 2001), UGC 8651 (Karachentsev et al. 2002), and UGC 9240 (Karachentsev et al. 2002)]; for those galaxies without TRGB distances, the distance to each system is calculated from the systemic velocity using a Virgocentric infall model and an H_0 of 75 km s $^{-1}$ Mpc $^{-1}$. Optical colors, sizes, luminosities, M_H/L_B , central surface brightnesses, and dynamical mass estimates listed in Table 1 are taken from the tabulation of van Zee (2000b). The absolute blue magnitudes and colors have been corrected for Galactic extinction, but not for internal extinction or for nebular

contributions to the broadband luminosity. Finally, the oxygen and nitrogen abundances tabulated in Table 1 are the mean values from the present study.

2.2. Optical Spectroscopy

Optical spectroscopic observations of H II regions in 21 dwarf irregular galaxies were obtained with the Double Spectrograph on the 5m Palomar¹ telescope during several observing runs between 1999 January and 2002 April. The observations were obtained in long-slit mode; the 2' long-slit was set to an aperture 2'' wide. The two sides of the spectrograph were set to complementary spectral resolution, and provided continuous wavelength coverage between 3600 Å and 7600 Å. The blue side was equipped with a 600 l/mm grating (spectral resolution of 5.0 Å or 1.72 Å pix⁻¹); the red side was equipped with a 300 l/mm grating (spectral resolution of 7.9 Å or 2.47 Å pix⁻¹). We also include observations of CGCG 007-025, which were obtained in 1997 January, during an observing run described in van Zee et al. (1998b).

The H α images of van Zee (2000b) were used to determine the appropriate slit positions and position angles (except for UGC 4483, where an H α image was kindly provided by Evan Skillman). Astrometric plate solutions were calculated using the coordinates of the bright stars in the APM catalog (Maddox et al. 1990), yielding positions accurate to within 1''. In all cases, the telescope was centered on a nearby star, and then moved to the H II region via blind offsets. The slit positions and position angles are tabulated in Table 2. The slit was set to a position angle close to the parallactic angle at the time of the observations. The observations were scheduled to maximize the number of H II regions that could be observed simultaneously. In some instances, faint H II regions were given higher priority if the parallactic angle was favorable for observations of multiple H II regions in a single slit position. In all, the 31 pointings yielded high signal-to-noise observations of 67 H II regions. Throughout this paper, the H II region nomenclature is based on east–west and north–south offsets from the galaxy center. These offsets are derived either from the pointing center (if only one H II region was in the slit), or are computed for each H II region from the pointing center, the slit position angle, and the spatial scale of the spectrum.

The long-slit optical spectra were processed using standard methods in the IRAF² package. The flat field was created from a combination of dome flats and twilight flats to correct for the slit illumination and wavelength responsivity. Wavelength rectification was based on arclamps taken before and after each series of observations. The images were rectified in the spatial dimension based on the trace of stars at different positions along the slit. One-dimensional (1-d) spectra were then extracted from the two dimensional images. Aperture sizes for the extracted 1-d spectra

¹Observations at the Palomar Observatory were made as part of a continuing cooperative agreement between Cornell University and the California Institute of Technology.

²IRAF is distributed by the National Optical Astronomy Observatories.

were matched to the observations: faint H II regions (isolated H II regions) were extracted with apertures defined at 10% of the peak, while brighter H II regions (H II region complexes) were extracted with both wide (10% of the peak) and narrow ($3''$) apertures. In the final analysis, the narrow ($3''$) apertures were favored for the bright H II regions since they had less contamination from blending. The one-dimensional spectra were flux calibrated using standard stars from the compilation of Oke (1990). Typical rms for the flux calibration is 0.015. While the nights were typically non-photometric, the relative line ratios should be robust. Representative spectra are shown in Figure 1. The excellent agreement in the continuum levels in the blue and red spectra illustrated in Figure 1 confirms that the extraction regions were well matched in the two cameras.

3. Nebular Abundances

3.1. Line Ratios and Diagnostic Diagrams

Analysis of the H II region line fluxes followed the same procedures as described in van Zee et al. (1997a) and van Zee et al. (1998b). Briefly, emission line strengths were measured in the 1-d spectra and then corrected for underlying Balmer absorption and for reddening. The intrinsic Balmer line strengths were interpolated from the tabulated values of Hummer & Storey (1987) for case B recombination, assuming $N_e = 100 \text{ cm}^{-3}$ and $T_e = T_{[\text{O III}]}$ (see Section 3.2). Assuming a value of $R = A_V/E_{B-V} = 3.1$, the galactic reddening law of Seaton (1979) as parameterized by Howarth (1983) was adopted to derive the reddening function, $f(\lambda)$, normalized at $\text{H}\beta$. For those H II regions with detected $[\text{O III}] \lambda 4363$, the temperature was then recalculated from the corrected line strengths and a new reddening coefficient was produced. An underlying Balmer absorption with an equivalent width of 2 \AA was assumed in the few instances where the reddening coefficient was significantly different when derived from the observed line ratios of $\text{H}\alpha/\text{H}\beta$ and $\text{H}\gamma/\text{H}\beta$.

The reddening corrected line intensities relative to $\text{H}\beta$ and the reddening coefficients, $c_{\text{H}\beta}$, for each H II region are listed in Table 3. In this and subsequent tables, each H II region is identified by its east–west and north–south offsets from the galaxy center (in arcsec, north and east are positive) and by its slit number (Table 2). The error associated with each relative line intensity was determined by taking into account the Poisson noise in the line, the error associated with the sensitivity function, the contributions of the Poisson noise in the continuum, read noise, sky noise, and flat fielding or flux calibration errors, the error in setting the continuum level (assumed to be 10% of the continuum level), and the error in the reddening coefficient.

All of the H II regions in this sample fall within the normal locus of line ratio values in standard diagnostic diagrams. For example, the ratio of $[\text{N II}]/[\text{O II}]$ is shown as a function of the strength of the strong oxygen lines ($R_{23} \equiv ([\text{O II}] + [\text{O III}])/\text{H}\beta$) in Figure 2. All of the H II regions in this sample have relatively weak $[\text{N II}]$ emission, as expected for low metallicity H II regions. Also included in Figure 2 are spiral galaxy H II regions (van Zee et al. 1998b) and H II regions in low surface brightness dwarf galaxies (van Zee et al. 1997a) which were observed and analyzed in a

similar manner to those in the present study. The high metallicity H II regions trace a narrow locus in this diagnostic diagram while the dwarf galaxy H II regions exhibit a wide range of $[\text{N II}]/[\text{O II}]$ for a given value of R_{23} . Such a range is expected for H II regions with a wide range of ionization parameters (e.g., McGaugh 1994, and see Section 3.4).

3.2. Temperature and Density Determinations

When possible, the electron temperature of the ionized gas is derived from the reddening corrected line strengths of the $[\text{O III}]$ $\lambda 5007$, $\lambda 4959$, and $\lambda 4363$ lines (Table 4). The procedure to determine the electron temperature of the O^{++} zone is well described in Osterbrock (1989) and will not be repeated here. A version of the FIVEL program of De Robertis, Dufour, & Hunt (1987) was used to compute T_e from the $[\text{O III}]$ line ratios. In addition, since numerical models of H II regions have shown that there are significant differences between the temperatures in the high- and low-ionization zones (Stasińska 1980), we adopt the approach taken by Pagel et al. (1992), who use the H II region models of Stasińska (1990) to derive an approximation of the electron temperature in the O^+ zone:

$$T_e(\text{O}^+) = 2[T_e^{-1}(\text{O}^{++}) + 0.8]^{-1}, \quad (1)$$

where T_e is the electron temperature in units of 10^4 K.

In many cases, $[\text{O III}]$ $\lambda 4363$ either is not detected or is contaminated by the nearby Hg $\lambda 4358$ night sky line. In these cases, we use ionization models to approximate the oxygen abundance and the electron temperature. Because oxygen is one of the dominant coolants in low metallicity H II regions, the electron temperature depends strongly on the oxygen abundance. Thus, we determine the electron temperature necessary to obtain the oxygen abundance as determined by strong-line methods (see Section 3.4) and adopt that value for subsequent analysis of other atomic abundance ratios. While the errors in the electron temperatures derived by this method are quite large, relative atomic abundances (such as N/O) are less sensitive to choice of electron temperature (e.g., Kobulnicky & Skillman 1996). We caution, however, that systematic errors in the strong-line abundance calibration will introduce systematic errors in these temperature estimates as well. For H II regions where the electron temperature was derived from the assumed oxygen abundance, the error in the electron temperature was set to yield the appropriate error (as determined by the calibration process) in the computed oxygen abundance. The electron temperatures for the O^{++} zone adopted for the subsequent abundance analysis are tabulated in Table 5.

The density sensitive line ratio $[\text{S II}]$ $\lambda 6717/6731$ is tabulated for each H II region in Table 4. The majority of the H II regions in this sample are within the low density limit ($I(\lambda 6717)/I(\lambda 6731) > 1.35$). In calculating the emissivities for the abundance analysis, an electron density of 100 cm^{-3} was assumed unless the $[\text{S II}]$ line ratios were below the low density limit, in which case the FIVEL program (De Robertis, Dufour, & Hunt 1987) was first used to calculate the electron density from the $[\text{S II}]$ line ratios.

3.3. Direct Oxygen Abundances

For H II regions with a solid detection of [O III] $\lambda 4363$, the oxygen abundances tabulated in Table 5 are derived from the observed line strengths (Table 3) and the relevant emissivity coefficients (based on the electron temperature (Table 5) and electron density) as calculated by the FIVEL program (De Robertis, Dufour, & Hunt 1987). Even in these relatively high signal-to-noise ratio spectra, the errors in the derived abundances are dominated by the errors inherent in the electron temperature derivation. Fourteen of the 21 galaxies in this sample have at least one H II region with a solid $\lambda 4363$ detection (25 H II regions in total). As found in other low mass galaxies (e.g., Kobulnicky & Skillman 1997), oxygen abundances derived from multiple H II regions within the same galaxies are quite similar (see Section 3.6 for further discussion). As the abundances calculated from direct detection of the temperature sensitive lines are less likely to be affected by significant systematic errors, these abundances are given more weight in the mean abundances tabulated in Table 1.

3.4. Strong-Line Oxygen Abundances

3.4.1. Photoionization Model Grids

The majority of spectra in this sample are of H II regions with low ionization parameters; thus, despite high signal-to-noise ratios in the strong lines, the [O III] $\lambda 4363$ line is often too weak to use to calculate the electron temperature directly. However, the behavior of the strong optical oxygen line intensities ([O II] $\lambda 3727$ and [O III] $\lambda\lambda 4959, 5007$) as a function of oxygen abundance has been examined extensively via semi-empirical methods (e.g. Searle 1971; Pagel et al. 1979; Alloin et al. 1979; Edmunds & Pagel 1984; Dopita & Evans 1986; Skillman 1989) and derived from H II region ionization models (e.g., McGaugh 1991; Olofsson 1997; Kewley & Dopita 2002). At low metallicities, the dominant coolant is the collisionally excited Lyman series, and thus the total oxygen line intensity (R_{23}) increases as the abundance increases. As the metallicity increases, however, the infrared fine structure lines, such as the 52μ and 88μ oxygen lines and the C^+ 158μ transition, begin to dominate the cooling. At an oxygen abundance of approximately 1/3 solar, the intensity of the optical oxygen lines reaches a maximum and then declines as the oxygen abundance increases. Thus, the relationship between R_{23} and oxygen abundance is double valued. As described by Alloin et al. (1979), this degeneracy can be broken with additional information, such as the relative strength of the nitrogen and oxygen lines. The low [N II]/[O II] line ratios (Table 4; Figure 2) indicate that all of the H II regions in the present sample are located on the lower branch of the R_{23} relation.

The lower branch of the theoretical model grid of McGaugh (1991) is shown in Figure 3. In this and other similar photoionization model calibration methods (e.g., Kewley & Dopita 2002), the geometry of the H II region (represented here by the average ionization parameter, \bar{U} , the ratio of

ionizing photon density to particle density) introduces a further spread in the estimated abundance for a given R_{23} . Thus, the process of determining an empirical abundance from the strong line ratios requires knowledge of both the total oxygen line intensity and the ratio of [O III] to [O II] to estimate the ionization parameter. Oxygen abundances derived from the photoionization model grid of McGaugh (1991) are tabulated for all of the H II regions in Table 5.

Most strong-line abundance calibrations are derived from photoionization models of zero-age H II regions (e.g. McGaugh 1991; Kewley & Dopita 2002). Thus, systematic abundance errors may be introduced when H II regions age, as both the ionization parameter and shape of the ionizing spectrum will evolve (e.g., Stasińska & Leitherer 1996; Olofsson 1997). As discussed in van Zee et al. (2005), such effects may be significant for H II regions with $\log ([\text{O III}]/[\text{O II}]) < -0.4$. In this sample, UGC 1175 -004+007, UGC 2023 -028+023, UGCA 292 +026+004, and UGC 9992 +007+010 all lie within this region of high uncertainty; however, due to the lack of detailed age information for these particular H II regions, we do not include age effects in the present analysis. Fortunately, several H II regions were observed in all four of these galaxies, and thus the tabulated mean abundances (Table 1) do not rely heavily on the results from these four extremely low ionization parameter H II regions.

3.4.2. Comparison of Direct and Strong Line Abundance Calibrations

As discussed in van Zee et al. (2005), the McGaugh (1991) photoionization models appear to trace out the appropriate shape for iso-metallicity contours in the abundance diagnostic diagram, but there is evidence of a systematic offset between direct and empirical calibration methods. For example, in Figure 3, the five H II regions in UGCA 292 form a tight locus around the $12+\log(\text{O}/\text{H}) = 7.35$ iso-metallicity contour while direct abundance calculations for 3 of these H II regions yield $12+\log(\text{O}/\text{H}) \sim 7.32 \pm 0.03$.

Figure 4 compares the direct abundance determinations (Section 3.3) with the strong line abundance determinations (Section 3.4.1) for the 25 H II regions in the present sample with high signal-to-noise ratio detections of [O III] $\lambda 4363$ as well as 12 H II regions from van Zee et al. (1997a) which were analyzed in a similar manner. The statistical offset between direct abundance calculations and the McGaugh (1991) model grid is -0.07 ± 0.10 dex for these 37 H II regions. If the high ionization parameter H II regions of Izotov et al. (1994), Thuan et al. (1995), Izotov et al. (1997), and Izotov & Thuan (1998) are also included, the statistical offset is -0.08 ± 0.11 dex. Thus, the McGaugh (1991) strong line abundance calibration appears to overpredict the oxygen abundance relative to direct abundance calculations. However, the statistical offset between direct abundances and McGaugh (1991) calibration does not appear to have systematic trends in regards to signal-to-noise ratio, oxygen abundance, or ionization parameter. Thus, to place the strong line abundances and direct abundances on the same approximate calibration scale, it may be appropriate to subtract 0.07 dex from the tabulated values.

Offsets between photoionization model grids and direct calibration methods have been noted by many authors; recently, Pilyugin (2000) proposed empirical calibrations based on H II regions where [O III] $\lambda 4363$ has been detected. However, such purely empirical calibrations potentially suffer from severe selection effects since the majority of high quality abundances available in the literature are biased toward H II regions with high ionization parameters, since these H II regions will have stronger [O III] line intensities for a given abundance. For example, H II regions in blue compact dwarf galaxies typically have ionization parameters between 0.01 and 0.1 (e.g., Izotov et al. 1997; Izotov & Thuan 1998). The present sample significantly extends the number of H II regions of moderate ionization parameters and direct abundance determinations. Similar to the H II regions in van Zee et al. (1997a), the H II regions in the present sample tend to have low average ionization parameters, $\bar{U} \sim 0.001 - 0.01$; only one H II region in this sample, CGCG 007-025 -004+000, has an ionization parameter comparable to H II regions in Izotov et al. (1997); Izotov & Thuan (1998).

The model grid for the Pilyugin (2000) empirical calibration based only on high ionization parameter H II regions (the p-method) is shown in Figure 3. In the high ionization parameter region, there is an offset of approximately 0.1 dex between the McGaugh (1991) and Pilyugin (2000) calibrations, as expected since the McGaugh (1991) photoionization model grid appears to overestimate the oxygen abundance by approximately this amount. However, in the lower ionization parameter regions of this diagnostic diagram, the Pilyugin (2000) empirical calibration deviates significantly from the photoionization grid, in a non-physical manner. Unfortunately, this is precisely the region of the diagnostic diagram where one is most likely to need to use a strong line abundance indicator, as the [O III] lines are weaker and thus the temperature sensitive lines will have lower signal-to-noise ratios.

A comparison of direct abundance calibrations and those derived by the p-method for the 37 moderate ionization parameter H II regions with solid [O III] $\lambda 4363$ detections (present sample; van Zee et al. 1997) is shown in Figure 4c. The p-method yields an oxygen abundance which is statistically 0.04 ± 0.11 dex lower than the direct abundance calculations in this sample. If the high ionization parameter blue compact dwarf galaxies of Izotov & Thuan are included, the statistical deviation of the p-method is 0.01 ± 0.14 dex (a lower statistical offset is expected when the blue compact dwarf galaxies are included since these same H II regions were used to derive the empirical calibration). However, as can be seen in Figure 4d, the deviation from the direct abundance calculations is strongly correlated with the ionization parameter. Thus, H II regions with high ionization parameters will be systematically underestimated by the p-method while H II regions with low ionization parameters (i.e., the most likely type of H II region for which a strong-line calibration will be needed) will be systematically overestimated by the p-method. Although the values are tabulated in Table 5, we elect not to use the p-method abundances for the H II regions in this sample due to these systematic calibration errors.

3.5. Relative Abundances of Nitrogen, Neon, Sulfur, and Argon

3.5.1. Ionization Correction Factors

For all atoms other than oxygen, derivation of atomic abundances requires the use of ionization correction factors (ICFs) to account for the fraction of each atomic species which is in an unobserved ionization state. To estimate the nitrogen abundance, we have assumed that $N/O = N^+/O^+$ (Peimbert & Costero 1969). To estimate the neon abundance, we have assumed that $Ne/O = Ne^{++}/O^{++}$ (Peimbert & Costero 1969). To determine the sulfur and argon abundances, we are forced to adopt an ICF from published H II region models to correct for the unobserved S^{+3} and Ar^{+3} states. We have adopted analytical forms of the ICFs as given by Thuan et al. (1995). Given the large uncertainties in the ICF, we do not report a sulfur abundance for H II regions where $S^{++} \lambda 6312$ is not detected.

3.5.2. Abundance Ratios

The abundance ratios of nitrogen, neon, sulfur, and argon relative to oxygen are tabulated in Table 5 and are shown graphically in Figure 5. Also include in these figures are additional dwarf irregular galaxy H II regions (van Zee et al. 1997a) and HII regions in spiral galaxies (van Zee et al. 1998b), all of which were analyzed in a similar manner. The H II regions in this sample range from those with extremely low metallicity (e.g., UGCA 292, $12 + \log(O/H) = 7.32$) to those that are a modest fraction of solar (e.g., UGC 3647, $12 + \log(O/H) = 8.07$).

As expected, the relative abundance ratios of the alpha elements (neon, sulfur, and argon) to oxygen is constant as a function of oxygen abundance. For this sample, the mean $\log(Ne/O)$ abundance ratio is -0.79 ± 0.09 , the mean $\log(S/O)$ is -1.53 ± 0.09 , and the mean $\log(Ar/O)$ is -2.19 ± 0.09 . These values are comparable to the values reported for starbursting dwarf galaxies (e.g., Thuan et al. 1995; Izotov et al. 1997; Izotov & Thuan 1998) and for other dwarf irregular galaxies (e.g., van Zee et al. 1997a).

At moderate and high metallicity, nitrogen is a secondary element ($\log(N/O)$ increases linearly with $\log(O/H)$, e.g., Torres–Peimbert et al. 1989; Vila–Costas & Edmunds 1993; Henry et al. 2000); however, at low metallicity, nitrogen behaves like a primary element with an approximately constant $\log(N/O)$ ratio for $12 + \log(O/H) < 8.3$ (e.g., Vila–Costas & Edmunds 1993; van Zee et al. 1998a; Henry et al. 2000). However, while the mean value is approximately constant at low metallicity, the range of observed $\log(N/O)$ increases significantly at $12 + \log(O/H) > 7.9$ (see also Kobulnicky & Skillman 1996, 1998). In this sample of H II regions, the mean $\log(N/O)$ ratio is -1.41 ± 0.15 , which is slightly higher than that found in extremely low metallicity H II regions (e.g., Thuan et al. 1995; Izotov et al. 1997; Izotov & Thuan 1998), but comparable to the observed values for several nearby low metallicity dIs (e.g., Skillman, Côté, & Miller 2003; Vílchez & Iglesias–Páramo 2003).

3.6. Global Abundances

Multiple H II regions were observed in 16 of the 21 galaxies. Figure 6 shows the observed oxygen abundances as a function of (normalized) galactic radius for the 12 galaxies with three or more observations which sample a range of galactic radii. In most instances, the derived elemental abundances are very similar (within the formal errors) within each galaxy. The one exception may be UGC 12894, but this plot may be misleading since the abundances of the inner H II regions are derived by the strong line method, and thus may be systematically too high (see Section 3.4). Thus, in most of these dwarf irregular galaxies both oxygen and nitrogen appear to be well mixed. Similar results have been found in other extensive studies of dwarf irregular galaxy abundances (e.g., Kobulnicky & Skillman 1996, 1997; Vílchez & Iglesias-Páramo 1998; Lee & Skillman 2004). Given their small dimensions and spatially homogeneous star formation histories (e.g., van Zee 2001), such uniform abundances are perhaps expected in dwarf irregular galaxies. Theoretical models of dispersal and mixing also suggest that the mixing time scales should be short, and that dwarf galaxies should be well mixed (e.g., Roy & Kunth 1995; Tenorio-Tagle 1996). Global oxygen and nitrogen-to-oxygen ratios are summarized in Table 1. In all instances, abundances derived from direct temperature measurements are given higher weight in the global averages.

Seven of the 21 galaxies in this sample have oxygen and nitrogen abundances previously reported. In general, the abundance measurements agree well for those galaxies with high signal-to-noise ratio observations both here and in the literature [UGC 4483, Skillman et al. (1994), CGCG 007-025, Kniazev et al. (2004); Izotov & Thuan (2004), and UGCA 292, (van Zee 2000a)]. However, the present observations indicate a slightly lower oxygen abundance for UGC 9240 (7.95 ± 0.03 as compared to 8.01 ± 0.03 , Hidalgo-Gómez & Olofsson 2002) despite both observations including detection of the temperature sensitive [O III] $\lambda 4363$ line. Finally, as expected for comparisons of direct and strong line abundances, the present observations yield significantly lower oxygen abundances for both UGC 2023 and UGC 3647 (Hunter & Hoffman 1999). It is important to note that despite the differences in absolute abundance calibration, the observations reported in Hunter & Hoffman (1999) also indicate that the oxygen abundances are spatially homogeneous in these two galaxies.

4. Chemical Enrichment of Gas-Rich Dwarf Irregular Galaxies

4.1. The Baseline Model: Closed Box Chemical Evolution

In the following discussion, the simple model of closed box chemical evolution will be used as the baseline for comparison of the observed chemical enrichment and theoretical models. As described in detail by Edmunds (1990), a simple closed box model sets the limit between the permitted and forbidden zones in abundance diagnostic diagrams. The simple closed box model assumes both instantaneous recycling and that the products of stellar nucleosynthesis are neither

diluted by infalling pristine gas nor lost to the system via outflow of enriched gas (e.g., Talbot & Arnett 1971; Searle & Sargent 1972). In a closed box model, the expected elemental abundance is related only to the yield (p) and the gas mass fraction (f):

$$z = p \ln (1/f) \quad (2)$$

where the gas mass fraction is the ratio of the gas mass to total baryonic mass of the system:

$$f = g/(g + s) \quad (3)$$

where g is the mass in gas and s is the mass in stars. The elemental yield is estimated from models of stellar nucleosynthesis and an initial mass function (IMF). Recent stellar evolution models indicate that for some elements, such as oxygen and nitrogen, the yield may be metallicity dependent and may depend on the stellar kinematics as well (e.g., rotation, Meynet & Maeder 2002). In the following discussion, we adopt a Salpeter (1955) IMF with an upper and lower limit of 120 and 2 M_{\odot} , respectively, and the integrated yields for stars with rotation from Meynet & Maeder (2002): $p_{\text{O}} = 7.4 \times 10^{-3}$ and $p_{\text{N}} = 1.1 \times 10^{-4}$. Changes in the upper mass limit of the IMF will primarily affect the yield of oxygen while changes in the lower mass limit of the IMF will primarily affect the yield of nitrogen. For the abundance range of interest ($12 + \log(\text{O}/\text{H}) < 8.4$), neither the oxygen nor the nitrogen yields are sensitive to metallicity for this choice of IMF (most modern stellar nucleosynthesis models now include primary nitrogen production at low metallicities, e.g., Timmes et al. 1995; Woosley & Weaver 1995; Meynet & Maeder 2002). However, while the ratio of N/O is only moderately affected, both oxygen and nitrogen yields are sensitive to the stellar kinematics; the stellar nucleosynthesis models with stellar rotation adopted here have higher yields than models without rotation.

A closed box enrichment model requires knowledge of both the gas mass and stellar mass. In this calculation, the gas mass includes the atomic component with a correction for neutral helium [$M_{\text{gas}} = 1.3 \times M_{\text{HI}}$], but does not include molecular gas since it is difficult to detect CO in low mass galaxies (e.g., Elmegreen, Elmegreen, & Morris 1980; Taylor, Kobulnicky, & Skillman 1998), and, further, the correction from CO to H_2 column density is highly uncertain for low metallicity galaxies (e.g., Verter & Hodge 1995; Wilson 1995). The stellar mass is derived from the B-band luminosity and the mass-to-light ratio calibration of van Zee (2001):

$$\log \Gamma_b = 2.84(B - V) - 1.26 \quad (4)$$

which was derived from the Bruzual & Charlot (1996) code for a quasi-continuous star formation rate model. We adopt the typical mass-to-light ratio of 0.75 ($B-V \sim 0.4$) for the handful of galaxies with no optical colors available.

A comparison of the observed oxygen abundances to those predicted by closed box models is shown in Figure 7. In this and subsequent figures, the galaxy sample includes both the present study and 19 galaxies from van Zee et al. (1997a, 2005) with distances converted to $H_0 = 75 \text{ km s}^{-1} \text{ Mpc}^{-1}$ for consistency (Table 6). While a large number of oxygen abundances now exist in the

literature (see, e.g., compilation in van Zee et al. 2005), at this time we restrict our analysis to this large uniform sample for which complementary deep optical and H I imaging exists.

Figure 7 indicates that several of the galaxies in this expanded sample are consistent with closed box chemical evolution (as also noted in van Zee et al. 1997b). However, the majority of galaxies in this sample appear to have oxygen abundances less than that expected by closed box models. The effective yield, p_{eff} , is defined as the yield that would be deduced if the galaxy was assumed to be a simple closed box. A histogram of the effective yields for this sample is shown in the bottom panel of Figure 7. The majority of galaxies appear to have an effective yield $\sim 1/4$ of the true yield ($p_{\text{eff}} \sim 0.002$).

While it is possible to minimize the offset between the closed box prediction and the observed abundances by tweaking the input model parameters, such efforts require either unusually high molecular-to-atomic gas ratios or unusually low stellar mass-to-light ratios. For instance, the majority of the galaxies can be brought into agreement with closed box chemical evolution models if we assume that the (unknown) molecular gas component is ~ 3 times the atomic component. Alternatively, the majority of the observations agree with a closed box estimate if the typical stellar mass-to-light ratio is 0.2. An intermediate result of $M_{H_2} \sim M_{HI}$ and $\Gamma_B \sim 0.4$ will also force the closed box model to fit the observations for the majority of the galaxies. However, even with adhoc adjustments of the input parameters, it is not possible to fit simultaneously all of the galaxies to a closed box model since those that previously appeared to be ‘closed’ are now overenriched relative to the model. Furthermore, none of these adhoc adjustments are motivated by physical processes. Thus, it appears that inflow of pristine gas or outflow of enriched gas may be the most straightforward explanation for the range of observed abundances in many low mass dwarf galaxies.

4.2. Effects of Gas Flows and Time Delays on Chemical Enrichment

An excellent overview of the effects of gas flows on observed chemical abundances is provided by Edmunds (1990). In brief, both infall and outflow of well mixed material will result in effective yields that are less than the true yields as the enriched material is either diluted (infall) or lost from the system (outflow). In this section, we discuss physical processes that can substantially affect chemical enrichment and summarize expected effects on the observed oxygen and nitrogen abundances. For the purposes of the following discussion, nitrogen will be considered a primary element, as appears to be appropriate at low metallicity (e.g., Edmunds & Pagel 1978).

(i) *Inflow of pristine gas.* If material added to the system is pristine, the effect of gas infall is to dilute the enriched gas and thus reduce the effective yield. Infall of pristine gas should have no effect on relative abundance ratios, such as N/O, since dilution is assumed to occur instantly and uniformly and both the oxygen and nitrogen abundances will be lower than predicted by closed box models. However, if a system undergoes significant infall, differences between closed box

abundances and observed abundances may be related to the gas mass fraction since galaxies with ‘excess’ gas may be more likely to have had significant infall.

(ii) *Infall of enriched gas.* If the new material added to the system is pre-enriched, the effect of infall depends on whether the metallicity is higher or lower than that of the system itself (e.g., Edmunds 1990). If the new material has lower metallicity, the effective yield will be less than the true yield. In addition, if the new material has similar abundance ratios as the existing gas (as is expected for primary elements, for example), the effect on relative abundance ratios, such as N/O, is minimal since the new and old material are similarly enriched. The effects are more complicated if the new material consists of both primary and secondary nitrogen [see Figure 2 of Edmunds (1990)].

(iii) *Outflow of enriched gas.* If the outflowing material is uniform and well mixed, the effective yield will be lower than the true yield and the abundance ratios, such as N/O, will be unchanged. Outflow of enriched gas can be the result of at least two distinct physical processes: (1) “blow-out” as a result of internal processes which inject kinetic energy in excess of the binding energy of the galaxy and (2) removal of the interstellar medium via external processes such as ram pressure stripping. In the former case, the observed abundances are lower than those predicted by closed box models because some of the enriched material is lost to the intergalactic medium. In the case of blow-out, one might expect a correlation between effective yield and either total mass (or mass surface density) or an anti-correlation with star formation rate. However, it should also be noted that despite their low mass, it appears to be quite difficult to remove fully the interstellar medium of typical dwarf irregular galaxies through internal processes such as blow-out (e.g., Mac Low & Ferrara 1999; Ferrara & Tolstoy 2000; Silich & Tenorio-Tagle 1998).

In the case of external triggers, the closed box model overpredicts the oxygen abundance because the gas mass fraction is now underestimated due to loss of the interstellar medium. Such enriched gas outflows could account for the enrichment patterns of dE/dSphs, which are both gas-poor and metal-poor (e.g., Mateo 1998). Furthermore, studies of abundance patterns of gas-rich galaxies in both cluster and field environments indicate that there are significant differences in the effective yields, as would be expected if the gas mass fractions of cluster galaxies are reduced due to ram pressure stripping (e.g., Skillman et al. 1996; Lee et al. 2003b). At the same time, however, global scaling relations, such as the metallicity-luminosity relation, may not be affected significantly by the environment (e.g., Lee et al. 2003b).

(iv) *Outflow of oxygen-rich gas from supernova winds.* In contrast to the previous case where the outflowing material is assumed to be well mixed, it is also possible that the outflowing gas is oxygen-rich since oxygen is formed in (short-lived) high mass stars and nitrogen is formed in (longer-lived) intermediate mass stars. If the enriched gas is lost via supernova winds, the effective yields of nitrogen and oxygen may no longer be coupled since recently enriched gas (oxygen-rich) is more likely to be ejected from the system. Differential outflow will result in higher N/O ratios than expected since oxygen is preferentially depleted. Nonetheless, even with differential outflow,

nitrogen may also be depleted since the outflow is likely to include the surrounding interstellar medium as well as the oxygen-rich ionized gas. However, with typical star formation rates of $\sim 0.001 - 0.01 \text{ M}_{\odot} \text{ yr}^{-1}$ (surface rates of 0.0001 to $0.001 \text{ M}_{\odot} \text{ yr}^{-1} \text{ kpc}^{-2}$), differential outflow may be less significant an issue for quiescent dwarf irregular galaxies. In contrast, starbursting dwarf galaxies (e.g., blue compact dwarf galaxies) will have periodic injections of substantial kinetic energy when their high mass stars evolve, and thus may experience substantial outflow of enriched material (e.g., NGC 1569, Martin, Kobulnicky, & Heckman 2002).

(v) *Extended gas distributions: inefficient mixing.* The standard closed box model assumes that all of the gas is involved in the chemical evolution. However, the HI distribution in most dwarf irregular galaxies extends at least a factor of two beyond the stellar disk (e.g., Broeils & Rhee 1997; Swaters et al. 2002; van Zee et al. 2004). If the outlying gas is not enriched by on-going star formation activity, the standard closed box model will underpredict the elemental abundances because the enriched material is mixing with a smaller fraction of the total gas mass (e.g., Gallagher & Hunter 1984). **Inefficient mixing is one of the few processes that result in effective yields which are higher than closed box yields.** If the extended gas distribution is significantly lower abundance than the inner gas, one might expect to see a correlation between effective yield and size of the HI disk.

Note that loss of pristine gas from the outer regions due to ram pressure stripping has similar results as described in (iii) since the overall gas mass fraction will be reduced, thereby increasing the predicted oxygen abundance.

(vi) *Time delay in delivery or mixing of products of stellar nucleosynthesis.* Because oxygen and nitrogen are formed in different mass stars, there may be a time delay between the observed enrichment of these two elements (e.g., Edmunds & Pagel 1978). Oxygen formed in Type II supernovae will be released after ~ 10 Myr while nitrogen will be produced and released over a substantially longer time period, ~ 250 Myr, as the intermediate mass stars evolve. Thus, if the products of stellar nucleosynthesis are mixed rapidly into the surrounding medium, one expects to see a rapid decrease in the N/O ratio when oxygen is released followed by a gradual increase in the N/O ratio as the intermediate mass stars have time to evolve and release nitrogen into the surrounding medium. Thus, the N/O ratio may act as a ‘clock’ marking the time since the last major star formation episode (e.g., Edmunds & Pagel 1978; Skillman, Bomans, & Kobulnicky 1997; Kobulnicky & Skillman 1998; Henry et al. 2000; Skillman, Côté, & Miller 2003).

4.3. Scaling Relations

4.3.1. Metallicity-Luminosity Relation

Relationships between global elemental abundances of both oxygen and nitrogen and absolute blue magnitude are shown in Figure 8. The derived slope (-0.149 ± 0.011) and intercept ($5.65 \pm$

0.17) for the oxygen metallicity-luminosity relationship for this sample are nearly identical to the relationship derived from a recent literature compilation for galaxies within 5 Mpc (van Zee et al. 2005) and to the field dwarf irregular sample of Lee et al. (2003a). The relationship derived from the 53000 galaxies in the SDSS data set is also consistent with the present observations, although their overall trend is steeper than that produced here (Tremonti et al. 2004).

In addition to intrinsic scatter due to galactic evolution (either chemical enrichment or luminosity evolution), the scatter in the observed luminosity-metallicity relationship may be due in part to the different oxygen abundance calibrations (direct vs strong line) or to errors in the adopted distances. First, as discussed in Section 3.4, the strong line abundance calibration used here for some of the H II regions may be systematically too high relative to direct abundance calculations. However, since the global abundances are weighted more heavily by H II regions with direct measurements, such effects should be relatively small for this sample. Systematic distance errors, which translate into incorrect absolute magnitudes, may be a more significant problem. For example, all of the galaxies which lie on the upper envelope of the oxygen abundance-luminosity relation are nearby galaxies with distances determined from TRGB observations (HKK L14, GR 8, UGC 9128, UGC 8651, UGC 9240, and UGC 685, in order of increasing luminosity) whereas the majority of distances in this study are estimated from Hubble flow models. A slight shift in the Hubble flow distances ($DM_{err} \sim 0.4$ magnitudes, or a 20% change in the distance estimate) could bring these points into better agreement.

The nitrogen abundance also has a strong correlation with the luminosity. The slope of the nitrogen abundance-luminosity correlation (-0.181 ± 0.014) is consistent with the slope of the oxygen abundance correlation. However, this relationship has significantly more scatter than the oxygen abundance-luminosity correlation (rms = 0.20 dex for N/H vs 0.15 dex for O/H). As can be seen in Figure 9, several of the galaxies in this sample have relatively high nitrogen-to-oxygen abundance ratios. The increased scatter in the observed nitrogen-to-oxygen abundance ratio at $12 + \log(\text{O}/\text{H}) > 7.9$ introduces additional scatter into the nitrogen abundance-luminosity correlation since galaxies with high N/O ratios do not fall in any preferred location in the oxygen abundance-luminosity diagram. We discuss N/O ratios in more detail below (Section 4.3.2).

The oxygen abundance-luminosity relation is the most commonly adopted abundance scaling relation since both parameters are easily obtained for large samples of galaxies (e.g., the large spectroscopic samples from SDSS, Tremonti et al. 2004). However, the underlying physical processes that drive these observed scaling relations may be more directly tied to a mass-metallicity correlation since more massive galaxies are both more efficient in converting gas into stars (lower gas mass fractions at the present epoch) and are able to retain a larger fraction of their processed metals due to their deeper gravitational potential wells. Nonetheless, the oxygen-luminosity relation is used as a first-order approximation since both stellar and dynamical masses are difficult to obtain: stellar mass estimates require knowledge of the underlying stellar population to determine a reliable mass-to-light ratio while dynamical masses require additional (time intensive) kinematic observations.

In Figure 10 we examine the residuals in the metallicity-luminosity relation as a function of dynamical mass, color, gas mass fraction, and surface brightness. While the dynamical mass estimates used here are approximate values based on global line widths, there is a suggestive trend that more massive galaxies have lower oxygen abundances than predicted by the metallicity-luminosity relation. This trend is in the opposite sense as one would expect for simple models of outflow or infall: the high mass galaxies are on the low side of the residuals suggesting that they are either underabundant or overluminous for their mass. Thus, the scatter in the metallicity-luminosity relationship is not easily identified as a result of either outflow (expected correlation with dynamical mass) or evolution (expected anti-correlation with gas mass fraction). It is also important to note that there is no correlation with central surface brightness, as one might expect if low surface brightness galaxies are less evolved than high surface brightness galaxies.

Finally, the fact that the nitrogen abundance relation has more scatter than the oxygen abundance-luminosity relation suggests that differential outflow (due to supernova winds, for example) may not be a significant cause of the lower effective yields and the high N/O ratios in dwarf irregular galaxies (Figure 7). In some regards, one might expect the nitrogen abundance to be a better tracer of the chemical enrichment history of a galaxy because it is formed in intermediate mass stars and thus is less likely to be lost from the system through outflow of enriched gas. In particular, differential outflow should introduce additional scatter in the oxygen abundance-luminosity relation since its efficiency will depend on a number of variables, such as the instantaneous star formation rate, mass surface density, and structure of the interstellar medium. The tightness of the oxygen luminosity-metallicity relation compared to the nitrogen relation suggests, however, that either the efficiency of differential outflow is common among all dwarf irregular galaxies or that its effects are negligible compared to evolutionary effects such as aging of the stellar population or time delay of delivery of enriched materials.

4.3.2. *N/O Ratios and Star Formation Histories*

The scatter in the N/O ratio at intermediate metallicities (Figure 9) has been attributed to several possible causes: (1) a time delay between release of oxygen and nitrogen; (2) additional production of secondary nitrogen; and (3) differential outflow of oxygen-rich gas. First, as discussed above (Section 4.3.1), differential outflow is unlikely to be the primary cause of the high N/O ratios in this sample because such a process predicts a tighter metallicity-luminosity relation for nitrogen (minimal outflow) than oxygen (outflow with variable efficiencies). Thus, while most of the galaxies in this sample appear to be open boxes (Section 4.1), the relative abundance ratios appear to be indicative of evolutionary effects rather than galactic processes (Section 4.2). Rather, the scatter in the observed N/O ratios may be due either to varied star formation rate histories or to the increasing production of secondary nitrogen at intermediate metallicities. For clarity, we initially discuss time delay issues for primary nitrogen alone (1) and then broaden the discussion to include the effects of additional synthetic pathways (2) on the observed abundance ratios.

We begin with a brief summary of the sources of primary and secondary nitrogen. At high metallicities, the nitrogen yield is linearly related to the initial metallicity (C and O) of the star; in other words, nitrogen is a secondary element and metal-rich stars will produce more nitrogen than metal-poor stars. Secondary nitrogen is produced in the core of intermediate mass stars during the CNO cycle (e.g., Clayton 1983). At low metallicities, however, nitrogen appears to be a primary element, i.e., produced only out of the original hydrogen in the star. Primary nitrogen may be produced in intermediate mass stars in which the C and O produced in the helium burning core is mixed into a hydrogen burning shell (e.g., Renzini & Voli 1981). Primary nitrogen may also be produced in low metallicity massive stars via convective overshoot (e.g., Timmes et al. 1995; Woosley & Weaver 1995). If primary nitrogen is produced in the same stars as oxygen, then the enrichment timescales for N and O are identical and the observed N/O ratio (for primary N) should be constant, regardless of overall oxygen abundance or age of the stellar population. However, if intermediate mass stars are the primary source of nitrogen, then there may be a significant time delay between oxygen enrichment and nitrogen enrichment; the length of the delay will depend both on stellar evolution timescales and on the cooling and mixing time of the enriched gas.

If the mixing timescales are short relative to stellar evolution, the scatter in the N/O vs O/H diagram may be a natural result of differing star formation histories. For example, a galaxy with a constant star formation rate will have a lower net nitrogen-to-oxygen yield than a galaxy with a declining star formation rate because more oxygen will have been released to the ISM due to the on-going star formation activity. Figure 9 shows the correlation in observed N/O ratio and the color of the underlying stellar population. While the color range is not large, a least-squares fit to the data yields:

$$\log(\text{N/O}) = 1.26(B - V)_0 - 1.96. \quad (5)$$

Also shown in Figure 9 are the mean values for 3 color bins; the mean $\log(\text{N/O})$ is -1.61 ± 0.14 for galaxies with $0.2 < B - V < 0.3$, -1.48 ± 0.11 for galaxies with $0.3 < B - V < 0.4$, and -1.41 ± 0.13 for galaxies with $0.4 < B - V < 0.5$. While degeneracy between age and metallicity of the dominant stellar population may introduce subtle effects in this diagram, the correlation between color and N/O ratio indicates that the high N/O ratios are a result of declining star formation rates. Note, however, that color is independent of dynamical mass and luminosity for this sample of galaxies. The correlation is well defined in Figure 9 in part because the present sample includes quiescent dwarf irregular galaxies with star formation histories that are well modelled by simple changes in the star formation rate. It is important to note that this scenario does not require star formation to occur in periodic starbursts. Rather, as long as the recent star formation activity is less than the past star formation rate, the delayed release of nitrogen from the aggregate intermediate mass stellar population will slowly increase the N/O ratio since it is not balanced by additional production of oxygen in high mass stars. While none exist in the present sample, it is also possible to create blue galaxies with high N/O ratios if one considers more complicated star formation histories; for example, if a major starburst episode begins after a long period of quiescence, the elemental abundances will be indicative of the previous enrichment history while the colors are indicative of the present star formation activity. Such pathological cases exist (e.g., NGC 5253, Kobulnicky et

al. 1997). Nonetheless, it is clear that high N/O ratios are correlated with redder systems and decreasing star formation rates for this representative sample of dwarf irregular galaxies.

If high N/O ratios are a natural result of the combined influences of varied star formation histories and delayed delivery of nitrogen from intermediate mass stars, then we would expect to see a range of N/O ratios at all metallicities since any red, low luminosity galaxy should have high N/O. However, to date, there are no known examples of extremely low metallicity galaxies with high N/O ratios. Rather, the N/O ratio appears to have minimal scatter until an oxygen abundance of $12 + \log \text{O/H} \sim 7.9$. In fact, Izotov & Thuan (1999) argue that the extremely small scatter in the N/O ratios of starbursting dwarf galaxies indicates that primary nitrogen is produced in massive stars (i.e., in the same stars that produce oxygen) and that extremely low metallicity galaxies are young (i.e., there has not been sufficient time since the onset of star formation for intermediate mass stars to evolve and release additional nitrogen). Since the low metallicity regime is precisely where we expect to be most sensitive to small increases in the nitrogen yield from intermediate mass stars, these observational results are difficult to explain in the context of normal star formation histories and chemical enrichment scenarios. Nonetheless, there are severe selection effects that bias current samples against red, low metallicity galaxies since the star formation rates of these galaxies will be extremely low; most metallicity studies (including this one) exclude galaxies with extremely faint HII regions since interpretation of the line ratios may be ambiguous (see Section 3.4). Nonetheless, observations of oxygen and nitrogen abundances in such low luminosity galaxies may be necessary to understand the true scatter in the N/O ratio, and thus to understand fully the chemical enrichment history of dwarf irregular galaxies.

Alternatively, the increased scatter in the N/O ratio may be a result of the increased importance of secondary nitrogen production as the metallicity of the system increases. Since secondary nitrogen is formed in intermediate mass stars, this scenario incorporates all of the aspects described above, but also introduces an additional free parameter: the effective yield of secondary nitrogen. Aside from the first generation of stars, any subsequent stellar population will include an increasing fraction of processed materials, and thus both primary and secondary nitrogen will be produced in intermediate mass stars. The point of inflection in the N/O plot at an oxygen abundance of $12 + \log(\text{O/H}) \sim 8.3$ is usually interpreted as the transition regime between secondary and primary nitrogen (e.g., Vila-Costas & Edmunds 1993; van Zee et al. 1998b; Henry et al. 2000). Since secondary nitrogen is formed in intermediate mass stars, a decreasing star formation rate will yield a high N/O ratio as more secondary nitrogen is slowly released into the interstellar medium without a corresponding increase in the oxygen abundance. Since the relative yields of primary and secondary nitrogen are metallicity dependent, this scenario predicts that the dispersion in N/O ratio should increase with oxygen abundance in the metallicity range where both primary and secondary processes are significant contributors to the nitrogen abundance.

Finally, as illustrated by Köppen & Hensler (2005), some of the scatter in the N/O ratio at intermediate metallicities may also be a result of global gas flows. As discussed in Section 4.2, infall or outflow of uniform, well mixed, material will not affect the observed N/O ratios. However,

Köppen & Hensler (2005) point out that infall of pristine gas onto a system that has already reached the secondary nitrogen regime may drive the system into the region of the abundance diagram populated by dwarf irregular galaxies since the oxygen abundance will be diluted but the N/O ratio remains unchanged. Assuming a reasonable mass distribution of such infall events also leads to a metallicity dependence in the dispersion of the N/O ratio. Thus, this scenario predicts that the observed scatter in the N/O ratio should be correlated with gas richness as infalling pristine gas will increase the gas mass fraction. However, the actual trend is in the opposite sense; galaxies with high gas mass fractions tend to have lower N/O ratios, while the high N/O ratios are found in systems with low gas mass fractions. In fact, all of the ‘closed box’ galaxies in this sample are on the lower envelope of observed N/O ratios. While this result may simply reflect that gas-rich systems are more likely to have continuous star formation activity, it argues against producing the observed scatter in N/O by diluting systems which have reached the secondary nitrogen regime.

Chemical evolution models which trace gas infall, outflow, star formation history, and enrichment patterns of all the elements may be necessary to disentangle fully the relative importance of time delays, secondary nitrogen production, and gas flows. At this time, several chemical enrichment models are able to reproduce the global trends in the nitrogen-to-oxygen abundance ratio at both low and high metallicities by invoking several different physical processes (e.g., Carigi et al. 1999; Larsen, Sommer-Larsen, & Pagel 2001; Mouhcine & Contini 2002; Köppen & Hensler 2005). A reasonable goal for future chemical evolution models is to produce both self-consistent star formation and chemical enrichment histories and to reproduce the scatter in observed abundance ratios.

4.4. Deviation from Closed Box Chemical Evolution

As discussed in Section 4.1, a handful of galaxies in this sample appear to be consistent with simple closed box chemical evolution; the majority, however, have lower effective yields than those predicted by closed box evolution and thus must have experienced significant gas infall or outflow. In this section, we examine global properties of dwarf irregular galaxies to investigate whether there are significant differences between ‘open’ and ‘closed’ systems. The effective yield is shown as a function of dynamical mass, absolute magnitude, M_H/L_B , and surface star formation rate (SFR/area) in Figure 11.

As discussed in Section 4.2, if the oxygen abundance is diluted significantly by infall of pristine gas, we expect to see a net anti-correlation between the effective yield and gas-richness since the infalling gas increases the total gas mass fraction of the system. However, as indicated in Figure 11c, this prediction is opposite to the trend observed. Rather, gas-rich galaxies appear to be closed systems while those with lower M_H/L_B have lower effective yields. Thus, as might be expected given the dearth of free floating HI clouds in the local universe, infall of pristine gas does not appear to be the dominant physical process that lowers the effective yields of dwarf irregular galaxies.

Discussions about the significance of gas infall in the chemical evolution of dwarf irregular galaxies are often complicated by the fact that many dIs are surrounded by large HI disks (e.g., Broeils & Rhee 1997; Swaters et al. 2002; van Zee et al. 2004). If the extended gas envelope has not been involved in the star formation process, this may be considered a potential source for infalling pristine gas (e.g., DDO 154 = UGC 8024, Kennicutt & Skillman 2001). However, in the context of this discussion, these extended gas disks should not be considered a source of pristine material since the closed box model presented here includes the *global* gas content. In other words, the extended gas disk has already been counted in the gas mass fraction; if only the gas associated with the stellar disk is considered, the effective yields are even lower than those presented here. Further analysis of the chemical enrichment process which includes detailed knowledge of the gas distribution and localized gas content (coincident with the stellar distribution, for example) is planned for a future paper.

The possibility that gas loss (outflow) drives the observed correlation between luminosity and metallicity has been considered in detail by both Garnett (2002) and Tremonti et al. (2004). Both of these studies indicate that massive gas-rich galaxies (spirals) are consistent with closed box chemical evolution while low mass galaxies appear to experience significant outflow. However, the galaxies in the present sample do not appear to confirm these trends (Figure 11a). Rather, the only apparent correlation between effective yield and global galaxy properties is with gas-richness; none of the other global parameters, including dynamical mass, absolute magnitude, current star formation activity, and surface brightness, have significant correlations with effective yield. Thus, while enriched gas outflow is a natural explanation for low effective yields in low mass galaxies, and some dwarf galaxies appear to have lost a significant fraction of their metals, there do not appear to be simple physical processes that dictate whether a galaxy will be an open or closed box.

5. Conclusions

We present the results of optical spectroscopy of 67 H II regions in 21 dwarf irregular galaxies. Elemental abundances of oxygen, nitrogen, neon, sulfur, and argon are derived and considered in the context of simple chemical evolution models. The major results are summarized below.

(1) Oxygen abundances are obtained via direct detection of the temperature sensitive lines for 25 H II regions (14 galaxies). The direct abundance calculations are compared with strong line abundance calibrations. The photoionization calibration of McGaugh (1991) yields a statistical offset of 0.07 dex, but the residuals have no apparent systematic trends. In contrast, while the empirical calibration of Pilyugin (2000) yields a negligible statistical offset for these H II regions, the residuals are correlated with ionization parameter. Thus, these observations indicate that oxygen abundances will be overestimated by the p-method for H II regions with low ionization parameters.

(2) H II region abundances are calculated at a range of radii for 12 of the 21 galaxies. In

general, oxygen abundances derived from observations of multiple H II regions within the same galaxy are quite similar, indicating that the interstellar medium is well mixed.

(3) Global elemental abundances for this sample of dwarf irregular galaxies are similar to those observed in other low mass dwarf galaxies. The mean $\log(\text{N/O})$ abundance ratio is -1.43 ± 0.15 , the mean $\log(\text{Ne/O})$ abundance ratio is -0.79 ± 0.09 , the mean $\log(\text{S/O})$ abundance ratio is -1.53 ± 0.09 , and the mean $\log(\text{Ar/O})$ abundance ratio is -2.19 ± 0.09 .

(4) The luminosity-metallicity relation for this sample of isolated dwarf irregular galaxies is: $12 + \log(\text{O/H}) = -0.149 M_B + 5.65$. The nitrogen abundance-luminosity relation is: $12 + \log(\text{N/H}) = -0.181 M_B + 3.69$. The nitrogen relation has significantly more scatter than the oxygen metallicity-luminosity relation.

(5) A correlation is found between the observed nitrogen-to-oxygen ratio and the color of the underlying stellar population in the sense that redder dwarf irregulars have higher N/O ratios than blue dwarf irregulars. This correlation is interpreted in the context of delayed release of nitrogen and varied star formation histories. The N/O ratio will gradually increase in galaxies with declining star formation rates as the newly released nitrogen from evolved intermediate mass stars will no longer be balanced by the influx of additional oxygen from recently formed high mass stars.

(6) Global oxygen and nitrogen abundances are examined in the context of open and closed box chemical evolution models. While several galaxies are consistent with closed box chemical evolution, the majority of this sample have an effective yield $\sim 1/4$ of the expected yield for a Salpeter IMF and constant star formation rate. However, the effective yield is not correlated with global galaxy parameters such as dynamical mass, absolute magnitude, star formation rate, or surface brightness. Rather, the effective yield is strongly correlated with M_H/L_B in the sense that gas-rich galaxies are more likely to be closed boxes.

We thank Evan Skillman for numerous discussions about dwarf galaxies and metallicity evolution. We thank Dick Henry and Henry Lee for helpful comments on early versions of this paper. This research has made use of the NASA/IPAC Extragalactic Database (NED) which is operated by the Jet Propulsion Laboratory, California Institute of Technology, under contract with the National Aeronautics and Space Administration. LvZ acknowledges partial support from the Herzberg Institute of Astrophysics and the National Research Council of Canada; LvZ also acknowledges partial support from Indiana University. MPH has been supported by NSF grants AST-9900695 and AST-0307396.

REFERENCES

- Alloin, D., Collin-Souffrin, S., Joly, M., & Vigroux, L. 1979, *A&A*, 78, 200
- Aparicio, A., Tikhonov, N., & Karachentsev, I. 2000, *aj*, 119, 177
- Broeils, A. H., & Rhee, M.-H. 1997, *A&A*, 324, 877
- Bruzual, A. G., & Charlot, S. 1996 in *AAS CD-ROM Series, Vol 7, Astrophysics on Disc* (Washington: AAS)
- Campbell, A., Terlevich, R. & Melnick, J. 1986, *MNRAS*, 223, 811
- Carigi, L., Colín, P., & Peimbert, M. 1999, *ApJ*, 514, 787
- Clayton, D. 1983, *Principles of Stellar Evolution and Nucleosynthesis* (Chicago, University of Chicago Press)
- De Robertis, M. M., Dufour, R. J., & Hunt, R. W. 1987, *JRASC*, 81, 195
- Dolphin, A. E., Makarova, L., et al. 2001, *MNRAS*, 324, 249
- Dohm-Palmer, R. C., et al. 1998, *AJ*, 116, 1227
- Dopita, M. A., & Evans, I. N. 1986, *ApJ*, 307, 431
- Edmunds, M. G. 1990, *MNRAS*, 246, 678
- Edmunds, M. G., & Pagel, B. E. J. 1978, *MNRAS*, 185, 77p
- Edmunds, M. G., & Pagel, B. E. J. 1984, *MNRAS*, 211, 507
- Elmegreen, B. G., Elmegreen, D. M., & Morris, M. 1980, *ApJ*, 240, 455
- Ferrara, A., & Tolstoy, E. 2000, *MNRAS*, 313, 291
- Gallagher, J. S., & Hunter, D. A. 1984, *ARA&A*, 22, 37
- Garnett, D. R. 1990, *ApJ*, 363, 142
- Garnett, D. R. 2002, *ApJ*, 581, 1019
- Henry, R. B. C., Edmunds, M. G., & Köppen, J. 2000, *ApJ*, 541, 660
- Hidalgo-Gómez, A. M., & Olofsson, K. 1998, *A&A*, 334, 45
- Hidalgo-Gómez, A. M., & Olofsson, K. 2002, *A&A*, 389, 836
- Howarth, I. D. 1983, *MNRAS*, 203, 301

- Hummer, D. G., & Storey, P. J. 1987, MNRAS, 224, 801
- Hunter, D. A., & Hoffman, L. 1999, AJ, 117, 2789
- Izotov, Yu. I., & Thuan, T. X. ApJ, 500, 188
- Izotov, Yu. I., & Thuan, T. X. ApJ, 511, 639
- Izotov, Yu. I., & Thuan, T. X. ApJ, 602, 200
- Izotov, Yu. I., Thuan, T. X., & Lipovetsky, V. A. 1994, ApJ, 435, 647
- Izotov, Yu. I., Thuan, T. X., & Lipovetsky, V. A. 1997, ApJS, 108, 1
- Karachentsev, I. D., Sharina, M. E., Makarov, D. I., Dolphin, A. E., Grebel, E. K., Geisler, D., Guhathakurta, P., Hodge, P. W., Karachentseva, V. E., Sarajedini, A., & Seitzer, P. 2002, A&A, 389, 812
- Karachentsev, I. D., Karachentseva, V. E., Huchtmeier, W. K., & Makarov, D. I. 2004, AJ, 127, 2031
- Kewley, L. J., & Dopita, M. A. 2002, ApJS, 142, 35
- Kennicutt, R. C., & Skillman, E. D. 2001, AJ, 121, 1461
- Kinman, T. D., & Davidson, K. 1981, ApJ, 243, 127
- Kniazev, A. Y., Pustilnik, S. A., Grebel, E. K., Lee, H. A., & Pramskij, A. G. 2004, ApJS, 153, 429
- Kobulnicky, H. A., & Skillman, E. D. 1996, ApJ, 471, 211
- Kobulnicky, H. A., & Skillman, E. D. 1997, ApJ, 489, 636
- Kobulnicky, H. A., & Skillman, E. D. 1998, ApJ, 497, 601
- Kobulnicky, H. A., Skillman, E. D., Roy, J.-R., Walsh, J. R., & Rosa, M. R. 1997, ApJ, 477, 679
- Kobulnicky, H. A., Willmer, C. N. A., Phillips, A. C. et al. 2003, ApJ, 499, 1006
- Köppen, J. & Hensler, G. 2005, A&A, 434, 531
- Larsen, T. I., Sommer-Larsen, J., & Pagel, B. E. J. 2001, MNRAS, 323, 555
- Lee, H., Grebel, E. K., & Hodge, P. W. 2003, A&A, 401, 141
- Lee, H., McCall, M. L., Kingsburgh, R. L., & Stevenson, C. C. 2003a, AJ, 125, 146
- Lee, H., McCall, M. L., & Richer, M. G. 2003b, AJ, 125, 2975

- Lee, H., & Skillman, E. D. 2004, *ApJ*, 614, 698
- Lee, J. C., Salzer, J. J., & Melbourne, J. 2004, *ApJ*, 616, 752
- Lequeux, J., Peimbert, M., Rayo, J. F., Serrano, A., & Torres-Peimbert, S. 1979, *A&A*, 80, 155
- Mac Low, M.–M., & Ferrara, A. 1999, *ApJ*, 513, 142
- Maddox, S. J., Sutherland, W. J., Efstathiou, G., & Loveday, J. 1990, *MNRAS*, 243, 692
- Maíz-Apellániz, J., Cieza, L., MacKenty, J. W. 2002, *AJ*, 123, 1307
- Martin, C. L., Kobulnicky, H. A., & Heckman, T. M. 2002, *ApJ*, 574, 663
- Mateo, M. L. 1998, *ARA&A*, 36, 435
- McGaugh, S. S. 1991, *ApJ*, 380, 140
- McGaugh, S. S. 1994, *ApJ*, 426, 135
- Maynet, G., & Maeder, A. 2002, *A&A*, 390, 561
- Miller, B. W., & Hodge, P. 1996, *ApJ*, 458, 467
- Mouhcine, M., & Contini, T. 2002, *A&A*, 389, 106
- Nilson, P., 1973, *Uppsala General Catalog of Galaxies (Uppsala) (UGC)*
- Oke, J. B. 1990, *AJ*, 99, 1621
- Olofsson, K. 1997, *A&A*, 321, 29
- Osterbrock, D. E. 1989, *Astrophysics of Gaseous Nebulae and Active Galactic Nuclei* (University Science Books, Mill Valley)
- Pagel, B. E. J., Edmunds, M. G., Blackwell, D. E., Chun, M. S., & Smith, G. 1979, *MNRAS*, 189, 95
- Pagel, B. E. J., Simonson, E. A., Terlevich, R. J., & Edmunds, M. G. 1992, *MNRAS*, 255, 325
- Peimbert, M., & Costero, R. 1969, *Bol. Obs. Tonantzintla y Tacubaya*, 5, 3
- Pilyugin, L. S. 2000, *A&A*, 362, 325
- Pilyugin, L. S. 2001, *A&A*, 374, 412
- Renzini, A., & Voli, M. 1981, *A&A*, 94, 175
- Richer, M. G., & McCall, M. L. 1995, *ApJ*, 445, 642

- Roy, J.-R., & Kunth, D. 1995, *A&A*, 294, 432
- Salpeter, E. E. 1955, *ApJ*, 121, 161
- Searle, L. 1971, *ApJ*, 168, 327
- Searle, L. & Sargent, W. L. W. 1972, *ApJ*, 173, 25
- Seaton, M. J. 1979, *MNRAS*, 185, 57P
- Silich, S. A., & Tenorio-Tagle, G. 1998, *MNRAS*, 299, 249
- Skillman, E. D. 1989, *ApJ*, 347, 883
- Skillman, E. D., Bomans, D. J., & Kobulnicky, H. A. 1997, *ApJ*, 474, 205
- Skillman, E. D., Côté, S., & Miller, B. W. 2003, *AJ*, 125, 610
- Skillman, E. D., Kennicutt, R. C., & Hodge, P. W. 1989, *ApJ*, 347, 875
- Skillman, E. D., Kennicutt, R. C., Shields, G. A., & Zaritsky, D. 1996, *ApJ*, 462, 147
- Skillman, E. D., Terlevich, R. J., Kennicutt, R. C., Garnett, D. R., & Terlevich, E. 1994, *ApJ*, 431, 172
- Stasińska, G. 1980, *A&A*, 84, 320
- Stasińska, G. 1990, *A&AS*, 83, 501
- Stasińska, G., & Leitherer, C. 1996, *ApJS*, 107, 661
- Swaters, R. A., van Albada, T. S., van der Hulst, J. M., & Sancisi, R. 2002, *A&A*, 390, 829
- Talbot, R. J. Jr., & Arnett, W. D. 1971, *ApJ*, 170, 409
- Taylor, C. L., Kobulnicky, H. A., & Skillman, E. D. 1998, *AJ*, 116, 2746
- Tenorio-Tagle, G. 1996, *AJ*, 111, 1641
- Thuan, T. X., Izotov, Y. I., & Lipovetsky, V. A. 1995, *ApJ*, 445, 108
- Timmes, F. X., Woosley, S. E., & Weaver, T. A. 1995, *ApJS*, 98, 617
- Torres-Peimbert, S., Peimbert, M., & Fierro, J. 1989, *ApJ*, 345, 186
- Tremonti, C. A., Heckman, T. M., Kauffmann, G. et al. 2004, *ApJ*, 613, 898
- van Zee, L. 2000a, *ApJ*, 543, L31
- van Zee, L. 2000b, *AJ*, 119, 2757

- van Zee, L. 2001, AJ, 121, 2003
- van Zee, L., Haynes, M. P., & Salzer, J. J. 1997a, AJ, 114, 2479
- van Zee, L., Haynes, M. P., & Salzer, J. J. 1997b, AJ, 114, 2497
- van Zee, L., Salzer, J. J., & Haynes, M. P. 1998, ApJ, 497, L1
- van Zee, L., Salzer, J. J., Haynes, M. P., O’Donoghue, A. A., & Balonek, T. J. 1998, AJ, 116, 2805
- van Zee, L., Skillman, E. D., & Haynes, M. P. 2004, AJ, 128, 121
- van Zee, L., Skillman, E. D., & Haynes, M. P. 2005, ApJ, in press
- Verter, F., & Hodge, P. W. 1995, ApJ, 446, 616
- Vila-Costas, M. B., & Edmunds, M. G. 1993, MNRAS, 265, 199
- Vílchez, J. M., & Iglesias-Páramo, J. 1998, ApJ, 508, 248
- Vílchez, J. M., & Iglesias-Páramo, J. 2003, ApJS, 145, 225
- Wilson, C.D. 1995, ApJ, 448, L97
- Woosley, S. E., & Weaver, T. A. 1995, ApJS, 101, 181

Table 1. Global Galaxy Parameters

Galaxy	RA (2000)	Dec (2000)	Morph. Type	Distance [Mpc]	R ₂₅ arcsec (kpc)	M _B	(B-V) ₀	M _H /L _B	μ_B^0	log(M _{dyn})	12 + log(O/H)	log(N/O)
UGC 12894	00 00 22.2	39 29 46.6	Im	7.9	21 (0.8)	-13.38	...	2.5	23.0	8.40	7.56 ± 0.04	-1.51 ± 0.10
UGC 290	00 29 07.9	15 54 02.9	Sdm	12.7	42 (2.6)	-14.48	0.31 ± 0.05	2.6	24.9	9.12	7.80 ± 0.10	-1.42 ± 0.11
UGC 685	01 07 22.4	16 41 04.3	SAm	4.79	44 (1.0)	-14.44	0.46 ± 0.02	0.8	21.5	9.08	8.00 ± 0.03	-1.45 ± 0.08
UGC 1104	01 32 42.4	18 19 00.9	Im	11.1	32 (1.7)	-16.08	0.40 ± 0.01	0.8	21.1	9.31	7.94 ± 0.05	-1.65 ± 0.14
UGC 1175	01 39 56.5	11 05 46.9	Sm:	11.3	18 (1.0)	-14.13	0.26 ± 0.04	6.6	22.5	9.08	7.82 ± 0.10	-1.50 ± 0.15
UGC 1281	01 49 31.4	32 35 16.6	SdM	4.6	136 (3.0)	-14.91	0.42 ± 0.03	1.4	23.9	9.37	7.78 ± 0.10	-1.29 ± 0.13
HKK97 L14	02 00 10.2	28 49 46.5	Irr	4.7	12 (0.3)	-11.26	...	0.5	24.3	7.48	7.65 ± 0.10	-1.26 ± 0.14
UGC 2023	02 33 18.6	33 29 28.7	Im:	10.2	44 (2.2)	-16.54	0.44 ± 0.04	0.6	22.8	9.23	8.02 ± 0.03	-1.35 ± 0.10
UGC 3647	07 04 50.0	56 31 09.8	IBm	19.7	40 (3.8)	-17.06	0.42 ± 0.03	1.4	21.8	9.68	8.07 ± 0.05	-1.28 ± 0.10
UGC 3672	07 06 27.3	30 19 21.1	Im	12.7	48 (3.0)	-15.43	0.27 ± 0.05	2.5	22.6	9.25	8.01 ± 0.04	-1.64 ± 0.12
UGC 4117	07 57 25.9	35 56 24.8	IBm	10.0	37 (1.8)	-14.86	0.31 ± 0.02	0.9	22.6	8.73	7.89 ± 0.10	-1.52 ± 0.15
UGC 4483	08 37 03.0	69 46 36.3	Im	3.21	34 (0.5)	-12.55	...	2.0	...	8.11	7.56 ± 0.03	-1.57 ± 0.07
CGCG 007-025	09 44 02.1	-00 38 32.6	Sm	17.8	15 (1.3)	-15.75	0.37 ± 0.02	1.3	20.5	9.36	7.83 ± 0.03	-1.48 ± 0.06
UGC 5288	09 51 17.0	07 49 40.0	Sdm:	5.3	37 (1.0)	-14.44	0.46 ± 0.06	1.8	20.6	9.22	7.90 ± 0.03	-1.42 ± 0.06
UGCA 292	12 38 39.7	32 45 49.3	ImIV-V	3.1	30 (0.4)	-11.43	0.08 ± 0.10	6.9	...	7.93	7.32 ± 0.06	-1.44 ± 0.10
UGC 8651	13 39 53.1	40 44 20.4	Im	3.01	69 (1.0)	-12.96	...	1.1	...	8.50	7.85 ± 0.04	-1.60 ± 0.09
UGC 9240	14 24 43.8	44 31 33.7	IAm	2.79	57 (0.8)	-13.96	0.37 ± 0.03	1.0	21.6	9.17	7.95 ± 0.03	-1.60 ± 0.06
UGC 9992	15 41 47.7	67 15 13.9	Im	8.6	32 (1.3)	-14.97	0.37 ± 0.04	1.2	22.8	8.44	7.88 ± 0.12	-1.26 ± 0.19
UGC 10445	16 33 47.6	28 59 05.1	SBe	15.1	60 (4.4)	-17.53	0.42 ± 0.03	1.0	21.8	10.24	7.95 ± 0.06	-1.20 ± 0.10
UGC 11755	21 29 59.6	02 24 50.8	BCD/E	18.0	27 (2.4)	-17.14	0.50 ± 0.03	0.1	22.6	9.76	8.04 ± 0.03	-1.10 ± 0.08
UGC 12713	23 38 14.4	30 42 30.6	S0/a	7.5	31 (1.1)	-14.76	0.46 ± 0.03	0.9	22.6	9.29	7.80 ± 0.06	-1.53 ± 0.10

Note. — Distances are calculated from systemic velocities using a Virgocentric infall model and an H_0 of 75 km s⁻¹ Mpc⁻¹ except for UGC 685 (Maíz-Apellániz et al. 2002), HKK97 L14 (Karachentzev et al. 2004), UGC 4483 (Dolphin et al. 2001), and UGC 8651 and UGC 9240 (Karachentzev et al. 2002), which have TRGB distances in the literature. Colors, magnitudes, optical size, and M_H/L_B are from van Zee (2000). Global oxygen and nitrogen abundances are from the present study except for UGC 3672, for which more accurate abundances are available in the literature (van Zee et al. 1997).

Table 2. Observing Log

Slit Position	RA (2000)	Dec (2000)	PA [deg]	Run	T _{int} [sec]
UGC 12894-A	00 00 23.8	39 29 43	89	Sep00	3 × 1200
UGC 290-A	00 29 08.3	15 53 57	135	Sep00	3 × 1200
UGC 685-A	01 07 22.8	16 40 53	334	Dec99	3 × 1200
UGC 685-B	01 07 23.2	16 41 00	41	Dec99	3 × 1200
UGC 1104-A	01 32 42.6	18 19 08	170	Dec99	3 × 1200
UGC 1104-B	01 32 42.7	18 19 00	109	Dec99	3 × 1200
UGC 1175-A	01 39 56.5	11 05 40	163	Sep00	3 × 1200
UGC 1281-A	01 49 32.1	32 35 30	90	Dec99	2 × 1200
HKK97 L14 -A	02 00 10.4	28 49 43	70	Dec99	3 × 1200
UGC 2023-A	02 33 15.7	33 29 19	80	Dec99	1 × 1200
UGC 2023-B	02 33 17.9	33 29 54	84	Dec99	3 × 1200
UGC 2023-C	02 33 18.1	33 29 51	93	Dec99	3 × 1200
UGC 3647-A	07 04 50.6	56 31 14	26	Dec99	1 × 1200
UGC 3672-A	07 06 23.3	30 20 52	106	Sep00	2 × 1200
UGC 4117-A	07 57 25.0	35 56 42	90	Mar00	5 × 1200
UGC 4117-B	07 57 25.8	35 56 33	110	Dec99	5 × 1200
UGC 4483-A	08 37 02.8	69 46 52	175	Dec99	1 × 1200
CGCG 007-025-A	09 44 01.8	−00 38 32	336	Jan97	1 × 900
UGC 5288-A	09 51 16.5	07 49 50	146	Dec99	3 × 1200
UGC 5288-B	09 51 17.4	07 49 27	9	Feb00	3 × 1200
UGC 5288-C	09 51 18.7	07 49 07	175	Dec99	5 × 1200
UGCA 292-C	12 38 40.0	32 46 02	112	Apr02	9 × 1200
UGCA 292-D	12 38 42.5	32 45 46	90	Apr02	4 × 1200
UGC 8651-A	13 39 57.0	40 44 56	90	Apr02	3 × 1200
UGC 9240-A	14 24 44.2	44 30 57	90	Apr01	3 × 1200
UGC 9992-A	15 41 50.0	67 15 02	165	Apr02	4 × 1200
UGC 10445-A	16 33 45.6	28 59 03	61	Apr01	2 × 1200
UGC 10445-B	16 33 46.1	28 59 53	110	Apr01	3 × 1200
UGC 11755-A	21 29 59.4	02 24 54	149	Sep00	2 × 1200
UGC 12713-A	23 38 14.3	30 42 28	90	Dec99	3 × 1200
UGC 12713-B	23 38 14.7	30 42 35	62	Dec99	1 × 1200

Table 3. HII Region Line Strengths

Galaxy/ Slit	Location EW NS	[OII] 3727+3729	[NeIII] 3869	[OIII] 4959+5007	[OI] 6300	[SIII] 6312	H α 6563	[NII] 6548+6584	He 6678	[SII] 6717+6731	[ArIII] 7136	$C_{H\beta}$	EW H β	H β [10^{-15}]
U12894/A	-006 -005	1.549 \pm 0.095	0.286 \pm 0.039	3.519 \pm 0.121	2.752 \pm 0.157	0.080 \pm 0.013	0.043 \pm 0.009	0.182 \pm 0.015	...	0.35 \pm 0.06	63	0.29
U12894/A	+004 -004	1.845 \pm 0.105	...	3.044 \pm 0.102	2.831 \pm 0.156	0.168 \pm 0.015	...	0.312 \pm 0.018	...	0.36 \pm 0.06	30	0.35
U12894/A	+018 -004	1.254 \pm 0.047	0.225 \pm 0.012	3.169 \pm 0.067	2.779 \pm 0.103	0.068 \pm 0.004	0.028 \pm 0.002	0.125 \pm 0.005	0.038 \pm 0.002	0.34 \pm 0.04	127	1.14
U290/A	-006 +006	2.238 \pm 0.202	...	1.493 \pm 0.107	2.828 \pm 0.250	0.145 \pm 0.023	...	0.326 \pm 0.029	...	0.40 \pm 0.09	10	0.16
U290/A	+006 -006	2.141 \pm 0.094	0.118 \pm 0.022	3.057 \pm 0.081	2.832 \pm 0.125	0.138 \pm 0.008	0.029 \pm 0.004	0.298 \pm 0.012	0.047 \pm 0.005	0.33 \pm 0.05	17	0.64
U685/A	+000 +001	2.446 \pm 0.103	0.513 \pm 0.029	6.048 \pm 0.144	2.809 \pm 0.124	0.169 \pm 0.009	0.024 \pm 0.004	0.547 \pm 0.019	0.082 \pm 0.006	0.11 \pm 0.05	12	1.34
U685/A	+006 -011	2.028 \pm 0.067	0.467 \pm 0.017	7.228 \pm 0.132	2.748 \pm 0.097	0.129 \pm 0.005	0.031 \pm 0.003	0.381 \pm 0.011	0.108 \pm 0.005	0.03 \pm 0.04	67	3.14
U685/B	+006 -011	2.057 \pm 0.073	0.460 \pm 0.019	7.218 \pm 0.139	2.773 \pm 0.103	0.146 \pm 0.006	0.029 \pm 0.003	0.377 \pm 0.011	0.098 \pm 0.005	0.07 \pm 0.04	59	3.35
U685/B	+012 -004	2.663 \pm 0.084	0.128 \pm 0.006	2.474 \pm 0.044	2.601 \pm 0.089	0.194 \pm 0.005	0.024 \pm 0.002	0.438 \pm 0.011	0.066 \pm 0.003	0.10 \pm 0.04	77	7.94
U1104/B	+002 +007	2.782 \pm 0.149	0.409 \pm 0.024	4.567 \pm 0.151	...	0.031 \pm 0.003	2.788 \pm 0.157	0.093 \pm 0.005	0.018 \pm 0.002	0.321 \pm 0.014	0.072 \pm 0.005	0.22 \pm 0.06	24	2.64
U1104/B	+004 -001	3.181 \pm 0.170	0.245 \pm 0.016	3.785 \pm 0.126	0.051 \pm 0.004	0.025 \pm 0.003	2.868 \pm 0.161	0.126 \pm 0.007	0.029 \pm 0.003	0.451 \pm 0.019	...	0.24 \pm 0.06	20	2.82
U1104/A	+004 -001	3.452 \pm 0.191	0.508 \pm 0.031	3.497 \pm 0.120	2.932 \pm 0.114	0.176 \pm 0.011	0.033 \pm 0.005	0.548 \pm 0.025	0.074 \pm 0.007	0.32 \pm 0.06	13	2.05
U1175/A	-004 +007	2.751 \pm 0.203	...	1.024 \pm 0.080	2.823 \pm 0.217	0.252 \pm 0.028	...	0.454 \pm 0.036	...	0.09 \pm 0.08	7	0.21
U1175/A	-002 -001	2.608 \pm 0.152	...	1.561 \pm 0.071	2.824 \pm 0.169	0.155 \pm 0.013	0.088 \pm 0.010	0.419 \pm 0.022	...	0.18 \pm 0.06	16	0.34
U1175/A	+000 -007	2.139 \pm 0.128	0.297 \pm 0.039	2.351 \pm 0.093	2.796 \pm 0.172	0.133 \pm 0.015	0.027 \pm 0.010	0.353 \pm 0.022	...	0.03 \pm 0.06	21	0.40
U1281/A	+008 +013	2.036 \pm 0.170	...	2.764 \pm 0.135	2.795 \pm 0.231	0.234 \pm 0.024	...	0.420 \pm 0.032	0.058 \pm 0.013	0.18 \pm 0.08	11	0.48
HKK L14/A	+002 -004	1.232 \pm 0.071	0.156 \pm 0.016	3.289 \pm 0.114	3.068 \pm 0.176	0.124 \pm 0.007	0.023 \pm 0.003	0.239 \pm 0.011	0.056 \pm 0.005	0.00 \pm 0.06	93	1.66
U2023/A	-036 -010	2.620 \pm 0.173	...	3.092 \pm 0.123	2.727 \pm 0.176	0.308 \pm 0.020	...	0.433 \pm 0.025	0.066 \pm 0.009	0.30 \pm 0.06	86	1.34
U2023/C	-029 +023	4.156 \pm 0.716	...	1.790 \pm 0.247	2.820 \pm 0.516	0.387 \pm 0.073	...	0.538 \pm 0.085	...	0.33 \pm 0.18	43	0.18
U2023/B	-028 +023	4.448 \pm 0.594	...	1.473 \pm 0.174	2.828 \pm 0.400	0.315 \pm 0.054	...	0.611 \pm 0.071	...	0.37 \pm 0.14	50	0.23
U2023/C	-020 +023	3.871 \pm 0.276	...	1.921 \pm 0.097	2.855 \pm 0.212	0.337 \pm 0.025	...	0.755 \pm 0.044	0.057 \pm 0.011	0.16 \pm 0.07	60	0.55
U2023/B	-014 +024	2.729 \pm 0.094	0.157 \pm 0.010	3.345 \pm 0.065	0.025 \pm 0.002	0.012 \pm 0.002	2.808 \pm 0.103	0.250 \pm 0.008	0.029 \pm 0.002	0.439 \pm 0.013	0.080 \pm 0.004	0.11 \pm 0.04	84	2.76
U2023/C	-013 +022	3.227 \pm 0.191	0.315 \pm 0.027	4.392 \pm 0.160	0.060 \pm 0.006	0.013 \pm 0.005	2.882 \pm 0.179	0.294 \pm 0.016	...	0.701 \pm 0.033	0.080 \pm 0.007	0.12 \pm 0.06	84	1.28
U2023/B	-008 +025	2.873 \pm 0.088	0.246 \pm 0.008	3.977 \pm 0.069	0.045 \pm 0.002	0.019 \pm 0.001	2.808 \pm 0.094	0.229 \pm 0.006	0.027 \pm 0.001	0.473 \pm 0.012	0.083 \pm 0.003	0.19 \pm 0.04	174	12.09
U2023/C	-006 +022	1.968 \pm 0.101	0.288 \pm 0.015	5.325 \pm 0.171	0.024 \pm 0.001	0.019 \pm 0.001	2.831 \pm 0.154	0.163 \pm 0.008	0.029 \pm 0.002	0.265 \pm 0.011	0.096 \pm 0.006	0.28 \pm 0.05	84	6.87
U2023/C	+028 +020	3.784 \pm 0.249	...	2.115 \pm 0.091	2.828 \pm 0.196	0.331 \pm 0.022	...	0.868 \pm 0.047	...	0.16 \pm 0.07	77	0.95
U3647/A	-006 -018	1.719 \pm 0.069	0.288 \pm 0.014	5.937 \pm 0.113	0.019 \pm 0.002	0.014 \pm 0.002	2.731 \pm 0.134	0.168 \pm 0.007	0.032 \pm 0.002	0.242 \pm 0.009	0.089 \pm 0.005	0.34 \pm 0.05	314	5.19
U3647/A	+004 +002	2.416 \pm 0.123	0.325 \pm 0.027	5.940 \pm 0.150	0.032 \pm 0.005	0.026 \pm 0.005	2.867 \pm 0.164	0.255 \pm 0.013	0.017 \pm 0.011	0.362 \pm 0.016	0.098 \pm 0.008	0.27 \pm 0.06	78	1.80
U3647/A	+006 +006	1.793 \pm 0.080	0.260 \pm 0.017	5.568 \pm 0.119	2.712 \pm 0.141	0.199 \pm 0.009	0.030 \pm 0.003	0.349 \pm 0.014	0.082 \pm 0.006	0.18 \pm 0.05	74	2.75
U3672/A	-052 +091	2.461 \pm 0.266	...	1.172 \pm 0.121	2.899 \pm 0.314	0.275 \pm 0.037	...	0.40 \pm 0.10	27	0.17
U4117/A	-011 +017	2.119 \pm 0.149	...	3.828 \pm 0.163	2.872 \pm 0.206	0.120 \pm 0.020	...	0.352 \pm 0.027	...	0.15 \pm 0.07	26	0.47
U4117/B	-001 +008	3.190 \pm 0.226	...	3.138 \pm 0.140	2.827 \pm 0.208	0.163 \pm 0.020	...	0.401 \pm 0.029	...	0.14 \pm 0.07	13	0.31
U4117/B	+012 +003	1.099 \pm 0.069	0.317 \pm 0.025	5.175 \pm 0.184	2.770 \pm 0.169	0.057 \pm 0.010	...	0.172 \pm 0.013	0.054 \pm 0.008	0.05 \pm 0.06	59	0.64
U4483/A	-001 +016	0.779 \pm 0.041	0.261 \pm 0.013	4.316 \pm 0.138	...	0.012 \pm 0.001	2.773 \pm 0.151	0.034 \pm 0.002	0.027 \pm 0.002	0.088 \pm 0.004	0.038 \pm 0.002	0.12 \pm 0.05	161	18.42
U4483/A	+001 -006	1.183 \pm 0.075	0.248 \pm 0.023	3.943 \pm 0.142	2.826 \pm 0.173	0.052 \pm 0.006	0.022 \pm 0.005	0.134 \pm 0.009	0.044 \pm 0.005	0.09 \pm 0.06	63	2.56
CGCG 007-025/A	-008 +007	1.207 \pm 0.050	0.340 \pm 0.015	5.800 \pm 0.132	0.025 \pm 0.002	0.022 \pm 0.002	2.807 \pm 0.128	0.065 \pm 0.003	0.026 \pm 0.002	0.194 \pm 0.007	0.041 \pm 0.002	0.22 \pm 0.05	179	6.19
CGCG 007-025/A	-004 +000	0.949 \pm 0.036	0.404 \pm 0.015	6.792 \pm 0.147	0.024 \pm 0.001	0.015 \pm 0.001	2.759 \pm 0.122	0.055 \pm 0.002	0.027 \pm 0.001	0.141 \pm 0.005	0.050 \pm 0.003	0.31 \pm 0.04	230	36.38
CGCG 007-025/A	+000 -009	1.242 \pm 0.050	0.369 \pm 0.016	5.340 \pm 0.120	0.028 \pm 0.002	0.019 \pm 0.001	2.894 \pm 0.131	0.074 \pm 0.004	0.027 \pm 0.002	0.171 \pm 0.006	0.040 \pm 0.002	0.12 \pm 0.05	68	7.56
U5288/A	-007 +010	2.130 \pm 0.111	0.407 \pm 0.021	5.240 \pm 0.168	0.044 \pm 0.003	0.020 \pm 0.002	2.817 \pm 0.154	0.204 \pm 0.009	0.027 \pm 0.002	0.531 \pm 0.022	0.089 \pm 0.006	0.17 \pm 0.05	84	6.87
U5288/A	-004 +006	2.921 \pm 0.153	0.395 \pm 0.021	4.769 \pm 0.155	0.060 \pm 0.004	0.017 \pm 0.003	2.819 \pm 0.156	0.256 \pm 0.011	0.022 \pm 0.003	0.636 \pm 0.027	0.083 \pm 0.006	0.21 \pm 0.05	32	6.05
U5288/A	-000 +000	3.410 \pm 0.187	0.223 \pm 0.017	3.956 \pm 0.136	2.813 \pm 0.162	0.310 \pm 0.016	0.021 \pm 0.005	0.669 \pm 0.030	0.090 \pm 0.008	0.16 \pm 0.06	18	2.06
U5288/B	+006 -013	3.940 \pm 0.179	0.633 \pm 0.038	4.344 \pm 0.119	0.096 \pm 0.010	0.037 \pm 0.010	2.750 \pm 0.131	0.280 \pm 0.018	...	0.842 \pm 0.033	0.096 \pm 0.010	0.16 \pm 0.05	11	2.34
U5288/A	+023 -034	2.577 \pm 0.191	0.276 \pm 0.043	5.333 \pm 0.231	2.828 \pm 0.215	0.085 \pm 0.020	...	0.296 \pm 0.028	0.102 \pm 0.017	0.15 \pm 0.07	-99	0.60
U5288/C	+026 -033	2.331 \pm 0.208	...	4.973 \pm 0.267	2.776 \pm 0.252	0.128 \pm 0.022	...	0.312 \pm 0.032	...	0.24 \pm 0.09	107	0.35
UA292/C	+008 +012	0.913 \pm 0.036	0.121 \pm 0.005	1.771 \pm 0.042	2.790 \pm 0.110	0.055 \pm 0.002	0.026 \pm 0.002	0.103 \pm 0.004	0.018 \pm 0.001	0.07 \pm 0.04	124	2.37
UA292/C	+026 +004	1.162 \pm 0.052	...	0.416 \pm 0.021	2.781 \pm 0.123	0.093 \pm 0.009	0.017 \pm 0.006	0.178 \pm 0.011	...	0.02 \pm 0.05	64	0.65
UA292/D	+035 -003	0.553 \pm 0.022	0.197 \pm 0.009	2.480 \pm 0.059	2.776 \pm 0.110	0.038 \pm 0.002	0.025 \pm 0.002	0.059 \pm 0.003	0.019 \pm 0.001	0.12 \pm 0.04	121	3.90
UA292/C	+038 +000	0.849 \pm 0.038	...	1.642 \pm 0.044	2.705 \pm 0.117	0.059 \pm 0.009	0.020 \pm 0.006	0.127 \pm 0.010	...	0.02 \pm 0.05	114	1.01
U8651/A	+045 +036	2.005 \pm 0.078	0.166 \pm 0.008	2.730 \pm 0.065	0.007 \pm 0.003	0.022 \pm 0.003	2.839 \pm 0.113	0.092 \pm 0.005	0.023 \pm 0.003	0.176 \pm 0.006	0.044 \pm 0.003	0.03 \pm 0.04	75	8.21
U9240/A	+004 -037	1.603 \pm 0.069	0.393 \pm 0.017	5.693 \pm 0.154										

Table 3—Continued

Galaxy/ Slit	Location EW NS	[OII] 3727+3729	[NeIII] 3869	[OIII] 4959+5007	[OI] 6300	[SIII] 6312	H α 6563	[NII] 6548+6584	He 6678	[SII] 6717+6731	[ArIII] 7136	$C_{H\beta}$	EW H β	H β [10 ⁻¹⁵]
U9992/A	+007 +010	2.676 \pm 0.262	...	0.865 \pm 0.105	2.745 \pm 0.281	0.280 \pm 0.037	...	0.749 \pm 0.065	...	0.00 \pm 0.10	47	0.24
U9992/A	+011 -003	1.943 \pm 0.094	0.177 \pm 0.022	3.756 \pm 0.111	2.805 \pm 0.137	0.199 \pm 0.012	0.026 \pm 0.006	0.578 \pm 0.024	0.056 \pm 0.007	0.13 \pm 0.05	47	0.82
U9992/A	+013 -012	3.518 \pm 0.155	0.079 \pm 0.017	1.611 \pm 0.048	2.830 \pm 0.129	0.293 \pm 0.013	0.020 \pm 0.005	0.767 \pm 0.027	0.055 \pm 0.006	0.15 \pm 0.05	35	1.36
U10445/B	-034 +053	3.300 \pm 0.399	...	5.395 \pm 0.414	2.860 \pm 0.367	0.407 \pm 0.069	...	0.721 \pm 0.088	...	0.06 \pm 0.12	107	0.25
U10445/A	-026 -002	3.001 \pm 0.132	0.176 \pm 0.010	2.722 \pm 0.077	0.055 \pm 0.003	0.017 \pm 0.002	2.793 \pm 0.122	0.374 \pm 0.013	0.027 \pm 0.002	0.623 \pm 0.021	0.075 \pm 0.004	0.05 \pm 0.05	81	5.66
U10445/B	-025 +050	3.277 \pm 0.255	...	1.672 \pm 0.106	2.482 \pm 0.202	0.353 \pm 0.036	...	0.844 \pm 0.058	...	0.00 \pm 0.08	31	0.51
U10445/B	-019 +048	3.462 \pm 0.148	0.221 \pm 0.011	2.865 \pm 0.080	0.106 \pm 0.005	0.015 \pm 0.002	2.785 \pm 0.117	0.363 \pm 0.012	0.026 \pm 0.002	0.782 \pm 0.024	0.065 \pm 0.004	0.04 \pm 0.04	98	5.64
U10445/B	-015 +047	3.173 \pm 0.142	0.198 \pm 0.013	2.843 \pm 0.082	0.077 \pm 0.005	0.011 \pm 0.003	2.802 \pm 0.126	0.390 \pm 0.014	0.032 \pm 0.003	0.771 \pm 0.027	0.068 \pm 0.005	0.02 \pm 0.05	95	2.98
U10445/B	-010 +045	3.714 \pm 0.229	...	2.811 \pm 0.116	2.811 \pm 0.179	0.347 \pm 0.022	...	0.522 \pm 0.029	0.062 \pm 0.010	0.22 \pm 0.06	96	8.97
U10445/A	-003 +010	3.349 \pm 0.273	...	2.486 \pm 0.142	0.124 \pm 0.021	...	2.840 \pm 0.241	0.538 \pm 0.045	...	0.414 \pm 0.037	...	0.14 \pm 0.08	20	0.63
U11755/A	-003 +003	2.067 \pm 0.067	0.246 \pm 0.008	4.307 \pm 0.082	0.023 \pm 0.002	0.014 \pm 0.001	2.809 \pm 0.096	0.310 \pm 0.009	0.031 \pm 0.002	0.385 \pm 0.010	0.103 \pm 0.004	0.22 \pm 0.04	45	21.56
U11755/A	-001 +000	2.938 \pm 0.099	0.301 \pm 0.012	3.287 \pm 0.065	0.051 \pm 0.003	0.013 \pm 0.003	2.821 \pm 0.100	0.487 \pm 0.015	0.031 \pm 0.003	0.784 \pm 0.022	0.084 \pm 0.004	0.23 \pm 0.04	12	7.33
U12713/B	-009 -003	1.644 \pm 0.090	...	3.403 \pm 0.092	2.671 \pm 0.156	0.073 \pm 0.009	0.034 \pm 0.007	0.267 \pm 0.015	0.043 \pm 0.007	0.22 \pm 0.06	22	1.76
U12713/A	-009 -003	1.623 \pm 0.084	...	3.552 \pm 0.093	2.790 \pm 0.160	0.092 \pm 0.015	0.022 \pm 0.011	0.249 \pm 0.019	0.036 \pm 0.011	0.18 \pm 0.06	25	0.91
U12713/A	-001 -003	2.122 \pm 0.083	0.197 \pm 0.012	3.277 \pm 0.064	2.803 \pm 0.138	0.098 \pm 0.007	0.026 \pm 0.004	0.300 \pm 0.012	0.053 \pm 0.005	0.25 \pm 0.05	42	2.18
U12713/B	+004 +004	2.163 \pm 0.088	...	2.128 \pm 0.045	2.711 \pm 0.136	0.117 \pm 0.007	0.019 \pm 0.004	0.404 \pm 0.016	...	0.17 \pm 0.05	29	4.34

Note. — EW of H β is listed in units of Å. H β flux is the observed quantity in units of erg s⁻¹ cm⁻²; no corrections have been applied for extinction and some observations were obtained in non-photometric conditions.

Table 4. HII Region Line Ratios

Galaxy/ Slit	Location EW NS	[SII] ratio	[OIII] ratio	Log [OII]+[OIII]	Log [OIII]/[OII]	Log [NII]/[OII]	Log [SII]/[OII]
U12894/A	-006 -005	1.53±0.26	...	0.705±0.013	0.356±0.031	-1.287±0.076	-0.930±0.045
U12894/A	+004 -004	1.28±0.15	...	0.689±0.013	0.217±0.029	-1.041±0.046	-0.772±0.035
U12894/A	+018 -004	1.40±0.11	60.9 ± 9.4	0.646±0.008	0.403±0.019	-1.266±0.030	-1.001±0.024
U290/A	-006 +006	1.23±0.22	...	0.577±0.026	-0.184±0.049	-1.188±0.079	-0.837±0.055
U290/A	+006 -006	1.55±0.13	...	0.716±0.010	0.155±0.022	-1.191±0.032	-0.856±0.026
U685/A	+000 +001	1.36±0.10	...	0.929±0.009	0.393±0.021	-1.161±0.030	-0.650±0.024
U685/A	+006 -011	1.35±0.08	81.2 ± 6.6	0.966±0.007	0.552±0.016	-1.196±0.022	-0.726±0.019
U685/B	+006 -011	1.45±0.09	85.9 ± 10.4	0.967±0.007	0.545±0.018	-1.149±0.024	-0.737±0.020
U685/B	+012 -004	1.39±0.07	88.4 ± 12.7	0.711±0.008	-0.032±0.016	-1.138±0.018	-0.784±0.018
U1104/B	+002 +007	1.45±0.12	86.2 ± 14.9	0.866±0.013	0.215±0.027	-1.476±0.033	-0.938±0.030
U1104/B	+004 -001	1.45±0.12	84.1 ± 17.0	0.843±0.013	0.076±0.027	-1.402±0.034	-0.848±0.030
U1104/A	+004 -001	1.36±0.12	...	0.842±0.014	0.006±0.028	-1.293±0.036	-0.799±0.021
U1175/A	-004 +007	1.82±0.30	...	0.577±0.025	-0.429±0.047	-1.038±0.058	-0.782±0.047
U1175/A	-002 -001	1.31±0.14	...	0.620±0.017	-0.223±0.032	-1.226±0.044	-0.794±0.034
U1175/A	+000 -007	1.89±0.25	...	0.652±0.015	0.041±0.031	-1.206±0.056	-0.782±0.038
U1281/A	+008 +013	1.47±0.23	...	0.681±0.020	0.133±0.042	-0.940±0.058	-0.686±0.049
HKK L14/A	+002 -004	1.32±0.13	...	0.655±0.013	0.426±0.029	-0.997±0.035	-0.712±0.032
U2023/A	-036 -010	1.27±0.15	...	0.757±0.016	0.072±0.034	-0.930±0.040	-0.782±0.038
U2023/C	-029 +023	1.30±0.41	...	0.774±0.055	-0.366±0.096	-1.031±0.111	-0.888±0.102
U2023/B	-028 +023	0.97±0.23	...	0.772±0.045	-0.480±0.077	-1.150±0.094	-0.862±0.077
U2023/C	-020 +023	1.32±0.15	...	0.763±0.022	-0.304±0.038	-1.060±0.045	-0.710±0.040
U2023/B	-014 +024	1.40±0.08	...	0.783±0.008	0.088±0.017	-1.038±0.020	-0.794±0.020
U2023/C	-013 +022	1.46±0.14	...	0.882±0.014	0.134±0.030	-1.040±0.035	-0.663±0.033
U2023/B	-008 +025	1.35±0.07	102.0 ± 8.0	0.836±0.007	0.141±0.015	-1.099±0.018	-0.783±0.017
U2023/C	-006 +022	1.35±0.11	106.5 ± 7.2	0.863±0.012	0.432±0.026	-1.082±0.031	-0.871±0.029
U2023/C	+028 +020	1.33±0.14	...	0.771±0.020	-0.253±0.034	-1.058±0.041	-0.639±0.037
U3647/A	-006 -018	1.44±0.11	116.4 ± 16.1	0.884±0.008	0.538±0.019	-1.010±0.025	-0.851±0.024
U3647/A	+004 +002	1.37±0.12	...	0.922±0.010	0.391±0.025	-0.977±0.031	-0.824±0.029
U3647/A	+006 +006	1.48±0.12	...	0.867±0.008	0.492±0.022	-0.955±0.028	-0.711±0.026
U3672/A	-052 +091	1.81±0.52	...	0.560±0.035	-0.322±0.065	...	-0.952±0.075
U4117/A	-011 +017	1.73±0.28	...	0.774±0.016	0.257±0.036	-1.247±0.079	-0.780±0.045
U4117/B	-001 +008	1.55±0.22	...	0.801±0.018	-0.007±0.036	-1.292±0.062	-0.901±0.044
U4117/B	+012 +003	1.05±0.16	...	0.798±0.014	0.673±0.031	-1.285±0.081	-0.805±0.043
U4483/A	-001 +016	1.38±0.11	56.0 ± 3.4	0.707±0.012	0.744±0.027	-1.360±0.034	-0.947±0.030
U4483/A	+001 -006	1.31±0.18	...	0.710±0.014	0.523±0.032	-1.357±0.057	-0.946±0.040
CGCG 007-025/A	-008 +007	1.40±0.10	71.6 ± 5.6	0.846±0.009	0.682±0.021	-1.269±0.027	-0.794±0.024
CGCG 007-025/A	-004 +000	1.31±0.09	60.1 ± 2.5	0.889±0.008	0.855±0.019	-1.237±0.023	-0.828±0.023

Table 4—Continued

Galaxy/ Slit	Location EW NS	[SII] ratio	[OIII] ratio	Log [OII]+[OIII]	Log [OIII]/[OII]	Log [NII]/[OII]	Log [SII]/[OII]
CGCG 007-025/A	+000 -009	1.34±0.10	82.1 ± 6.6	0.818±0.009	0.633±0.020	-1.225±0.029	-0.861±0.023
U5288/A	-007 +010	1.37±0.11	77.0 ± 6.2	0.867±0.012	0.391±0.027	-1.019±0.030	-0.603±0.029
U5288/A	-004 +006	1.50±0.12	73.4 ± 8.2	0.886±0.012	0.213±0.027	-1.057±0.029	-0.662±0.029
U5288/A	-000 +000	1.35±0.12	77.6 ± 18.4	0.867±0.014	0.065±0.028	-1.041±0.033	-0.707±0.031
U5288/B	+006 -013	1.49±0.12	...	0.918±0.011	0.042±0.023	-1.148±0.034	-0.670±0.026
U5288/A	+023 -034	1.53±0.30	...	0.898±0.016	0.316±0.037	-1.482±0.107	-0.940±0.052
U5288/C	+026 -033	0.87±0.18	...	0.864±0.020	0.329±0.045	-1.260±0.084	-0.873±0.059
UA292/C	+004 +013	1.36±0.09	54.4 ± 3.2	0.438±0.009	0.444±0.020	-1.144±0.024	-0.931±0.023
UA292/C	+008 +012	1.58±0.11	61.1 ± 6.5	0.429±0.009	0.288±0.020	-1.220±0.023	-0.948±0.024
UA292/C	+026 +004	1.44±0.18	...	0.198±0.015	-0.446±0.030	-1.097±0.046	-0.815±0.033
UA292/D	+035 -003	1.57±0.16	51.7 ± 4.5	0.482±0.009	0.652±0.020	-1.163±0.029	-0.972±0.028
UA292/C	+038 +000	1.59±0.27	...	0.396±0.010	0.286±0.023	-1.158±0.069	-0.825±0.039
U8651/A	+045 +036	1.38±0.10	109.2 ± 17.7	0.675±0.009	0.134±0.020	-1.338±0.029	-1.057±0.022
U9240/A	+004 -037	1.43±0.09	90.4 ± 6.2	0.863±0.010	0.550±0.022	-1.336±0.026	-0.962±0.024
U9992/A	+007 +010	1.81±0.31	...	0.549±0.035	-0.490±0.068	-0.980±0.072	-0.553±0.057
U9992/A	+011 -003	1.44±0.12	98.8 ± 52.1	0.756±0.011	0.286±0.025	-0.990±0.034	-0.526±0.028
U9992/A	+013 -012	1.49±0.11	...	0.710±0.014	-0.339±0.027	-1.079±0.027	-0.662±0.025
U10445/B	-034 +053	1.33±0.33	...	0.939±0.029	0.213±0.062	-0.909±0.091	-0.661±0.075
U10445/A	-026 -002	1.46±0.10	104.7 ± 24.3	0.758±0.012	-0.042±0.023	-0.904±0.024	-0.683±0.024
U10445/B	-025 +050	1.44±0.20	...	0.695±0.024	-0.292±0.044	-0.968±0.056	-0.589±0.045
U10445/B	-019 +048	1.40±0.09	...	0.801±0.012	-0.082±0.022	-0.979±0.023	-0.646±0.023
U10445/B	-015 +047	1.49±0.10	101.5 ± 32.8	0.779±0.012	-0.048±0.023	-0.910±0.025	-0.614±0.025
U10445/B	-010 +045	1.50±0.16	...	0.815±0.017	-0.121±0.032	-1.030±0.038	-0.852±0.036
U10445/A	-003 +010	1.29±0.23	...	0.766±0.023	-0.129±0.043	-0.794±0.051	-0.908±0.053
U11755/A	-003 +003	1.48±0.08	134.6 ± 8.8	0.804±0.007	0.319±0.016	-0.824±0.019	-0.730±0.018
U11755/A	-001 +000	1.48±0.08	109.6 ± 25.7	0.794±0.008	0.049±0.017	-0.781±0.020	-0.574±0.019
U12713/B	-009 -003	1.50±0.17	...	0.703±0.011	0.316±0.027	-1.353±0.059	-0.789±0.034
U12713/A	-009 -003	2.00±0.34	...	0.714±0.011	0.340±0.025	-1.247±0.074	-0.814±0.040
U12713/A	-001 -003	1.46±0.12	84.0 ± 19.4	0.732±0.008	0.189±0.019	-1.336±0.035	-0.850±0.024
U12713/B	+004 +004	1.40±0.11	...	0.633±0.010	-0.007±0.020	-1.267±0.031	-0.729±0.025

Note. — [S II] ratio = I(6717)/I(6731); [O III] ratio = I(4959+5007)/I(4363).

Table 5. HII Region Abundances

Galaxy	Location EW NS	T _e [OIII] K	12+	12+	12 + Log O/H	Log N/O	Log Ne/O	Log S/O	Log Ar/O
			Log(O/H) McGaugh	Log(O/H) Pilyugin					
U12894	-006 -005	14500 ± 2000	7.72	7.65	7.71± 0.10	-1.52± 0.14	-0.69± 0.24
U12894	+004 -004	13900 ± 2000	7.75	7.71	7.75± 0.10	-1.37± 0.15
U12894	+018 -004	15900 ± ¹³⁹⁰ ₁₀₂₀	7.65	7.54	7.56± 0.04	-1.54± 0.08	-0.77± 0.12	...	-2.25± 0.10
U290	-006 +006	12500 ± 1500	7.75	7.89	7.75± 0.10	-1.57± 0.16
U290	+006 -006	13200 ± 1500	7.82	7.79	7.82± 0.10	-1.45± 0.11	-1.00± 0.22	...	-2.28± 0.15
U685	+000 +001	11500 ± 1500	8.18	7.95	8.18± 0.10	-1.46± 0.15	-0.89± 0.28	...	-2.23± 0.18
U685	+006 -011	13970 ± ⁵⁰⁰ ₄₃₀	8.25	7.94	8.00± 0.03	-1.45± 0.06	-0.78± 0.07	...	-2.08± 0.08
U685	+006 -011	13630 ± ⁷⁹⁰ ₆₁₀	8.25	7.94	8.02± 0.04	-1.40± 0.07	-0.79± 0.10	...	-2.12± 0.09
U685	+012 -004	13490 ± ⁹³⁰ ₆₉₀	7.90	7.93	7.81± 0.04	-1.38± 0.07	-0.87± 0.11	...	-2.11± 0.09
U1104	+002 +007	13630 ± ¹¹⁴⁰ ₈₃₀	8.08	7.96	7.94± 0.05	-1.70± 0.09	-0.64± 0.13	-1.42± 0.12	-2.24± 0.10
U1104	+004 -001	13780 ± ¹⁴¹⁰ ₉₈₀	8.08	8.03	7.93± 0.05	-1.63± 0.11	-0.78± 0.14
U1104	+004 -001	11500 ± 1500	8.10	8.09	8.10± 0.10	-1.60± 0.14	...	-1.41± 0.25	-2.23± 0.17
U1175	-004 +007	11200 ± 1500	7.85	8.17	7.85± 0.10	-1.44± 0.17
U1175	-002 -001	12200 ± 1500	7.82	7.99	7.81± 0.10	-1.51± 0.13
U1175	+000 -007	13500 ± 1800	7.75	7.78	7.75± 0.10	-1.55± 0.15	-0.50± 0.25
U1281	+008 +013	13100 ± 1500	7.78	7.75	7.78± 0.10	-1.29± 0.13	-2.14± 0.17
HKK L14	+002 -004	14500 ± 2000	7.65	7.54	7.65± 0.10	-1.26± 0.14	-0.91± 0.24	...	-2.08± 0.16
U2023	-036 -010	12500 ± 1500	7.92	7.91	7.92± 0.10	-1.20± 0.13	-2.18± 0.16
U2023	-029 +023	10400 ± 1200	8.15	8.38	8.14± 0.11	-1.39± 0.18
U2023	-028 +023	9800 ± 1000	8.20	8.52	8.20± 0.10	-1.51± 0.17
U2023	-020 +023	11800 ± 1500	8.00	8.29	8.00± 0.10	-1.39± 0.14	-2.17± 0.19
U2023	-014 +024	12600 ± 1500	7.95	7.94	7.95± 0.10	-1.30± 0.12	-0.90± 0.23	-1.62± 0.17	-2.14± 0.15
U2023	-013 +022	11600 ± 1500	8.15	8.05	8.15± 0.10	-1.33± 0.14	-0.70± 0.27	-1.62± 0.21	-2.26± 0.17
U2023	-008 +025	12750 ± ⁴¹⁰ ₃₅₀	8.03	7.97	8.00± 0.03	-1.36± 0.06	-0.78± 0.07	-1.53± 0.07	-2.18± 0.07
U2023	-006 +022	12530 ± ³⁶⁰ ₃₀₀	7.98	7.84	8.02± 0.03	-1.35± 0.06	-0.84± 0.07	-1.54± 0.07	-2.08± 0.08
U2023	+028 +020	11500 ± 1500	8.07	8.24	8.07± 0.10	-1.35± 0.14
U3647	-006 -018	12140 ± ⁷⁰⁰ ₅₄₀	7.97	7.82	8.07± 0.04	-1.28± 0.07	-0.88± 0.10	-1.64± 0.11	-2.10± 0.09
U3647	+004 +002	12000 ± 1500	8.15	7.94	8.14± 0.10	-1.25± 0.13	-0.83± 0.25	-1.46± 0.23	-1.96± 0.16
U3647	+006 +006	13100 ± 1500	7.98	7.82	7.97± 0.10	-1.21± 0.12	-0.91± 0.21	...	-2.12± 0.15
U3672	-052 +091	12000 ± 1500	7.78	8.02	7.78± 0.10
U4117	-011 +017	13100 ± 1500	7.88	7.80	7.89± 0.10	-1.45± 0.14
U4117	-001 +008	12200 ± 1500	8.00	8.04	8.00± 0.10	-1.58± 0.14
U4117	+012 +003	14500 ± 2000	7.79	7.65	7.79± 0.10	-1.52± 0.16	-0.82± 0.24	...	-2.16± 0.17
U4483	-001 +016	16520 ± ⁵⁹⁰ ₄₅₀	7.62	7.50	7.56± 0.03	-1.57± 0.07	-0.84± 0.07	-1.62± 0.08	-2.18± 0.08
U4483	+001 -006	14700 ± 2000	7.70	7.58	7.69± 0.09	-1.59± 0.13	-0.80± 0.24	...	-2.22± 0.17
CGCG 007-025	-008 +007	14770 ± ⁵³⁰ ₅₀₀	7.86	7.72	7.83± 0.03	-1.55± 0.07	-0.83± 0.08	-1.47± 0.08	-2.33± 0.08
CGCG 007-025	-004 +000	16010 ± ³⁴⁰ ₃₃₀	7.89	7.74	7.78± 0.03	-1.47± 0.06	-0.84± 0.06	-1.63± 0.07	-2.20± 0.07
CGCG 007-025	+000 -009	13920 ± ⁵⁰⁰ ₄₃₀	7.82	7.70	7.86± 0.03	-1.47± 0.07	-0.76± 0.08	-1.51± 0.08	-2.34± 0.08
U5288	-007 +010	14320 ± ⁵¹⁰ ₅₀₀	8.00	7.86	7.90± 0.03	-1.26± 0.07	-0.71± 0.07	-1.51± 0.08	-2.12± 0.08
U5288	-004 +006	14570 ± ⁸⁴⁰ ₁₂₇₀	8.12	8.00	7.92± 0.05	-1.28± 0.08	-0.68± 0.13	-1.58± 0.33	-2.21± 0.10
U5288	-000 +000	14270 ± ¹⁸⁵⁰ ₁₂₀₀	8.15	8.08	7.90± 0.06	-1.28± 0.10	-0.84± 0.17	...	-2.13± 0.12
U5288	+006 -013	11000 ± 1500	8.30	8.17	8.26± 0.10	-1.54± 0.16	-2.24± 0.19
U5288	+023 -034	12200 ± 1500	8.10	7.95	8.09± 0.10	-1.76± 0.18	-0.87± 0.25	...	-2.12± 0.18
U5288	+026 -033	12500 ± 1500	8.02	7.89	8.02± 0.10	-1.53± 0.16

Table 5—Continued

Galaxy	Location EW NS	$T_e[\text{OIII}]$ K	12+	12+	12 + Log O/H	Log N/O	Log Ne/O	Log S/O	Log Ar/O
			Log(O/H) McGaugh	Log(O/H) Pilyugin					
UA292	+004 +013	$16820 \pm \frac{530}{470}$	7.38	7.22	7.30 ± 0.03	-1.45 ± 0.07	-0.82 ± 0.07	...	-2.32 ± 0.07
UA292	+008 +012	$15840 \pm \frac{920}{700}$	7.40	7.29	7.36 ± 0.04	-1.43 ± 0.07	-0.78 ± 0.09	...	-2.37 ± 0.08
UA292	+026 +004	12200 ± 1500	7.40	7.64	7.40 ± 0.10	-1.38 ± 0.13
UA292	+035 -003	$17230 \pm \frac{870}{710}$	7.38	7.20	7.31 ± 0.03	-1.37 ± 0.07	-0.73 ± 0.08	...	-2.30 ± 0.08
UA292	+038 +000	14700 ± 2000	7.39	7.24	7.40 ± 0.10	-1.40 ± 0.14
U8651	+045 +036	$12450 \pm \frac{850}{680}$	7.78	7.73	7.85 ± 0.04	-1.60 ± 0.09	-0.79 ± 0.12	-1.37 ± 0.12	-2.28 ± 0.10
U9240	+004 -037	$13350 \pm \frac{420}{330}$	7.92	7.79	7.95 ± 0.03	-1.60 ± 0.06	-0.75 ± 0.07	-1.60 ± 0.08	-2.15 ± 0.08
U9992	+007 +010	11200 ± 1500	7.85	8.21	7.84 ± 0.11	-1.29 ± 0.16
U9992	+011 -003	$12890 \pm \frac{5340}{1800}$	7.82	7.76	7.88 ± 0.12	-1.26 ± 0.19	-0.90 ± 0.34	...	-2.23 ± 0.23
U9992	+013 -012	11200 ± 1500	8.00	8.25	8.00 ± 0.10	-1.39 ± 0.16	-0.86 ± 0.30	...	-2.13 ± 0.19
U10445	-034 +053	10500 ± 2000	8.30	8.07	8.29 ± 0.20	-1.24 ± 0.24
U10445	-026 -002	$12620 \pm \frac{1400}{930}$	7.95	8.01	7.95 ± 0.06	-1.18 ± 0.09	-0.75 ± 0.16	...	-2.13 ± 0.12
U10445	-025 +050	11200 ± 1500	7.98	8.18	7.97 ± 0.10	-1.25 ± 0.17
U10445	-019 +048	12000 ± 1500	8.05	8.11	8.05 ± 0.10	-1.26 ± 0.13	-0.66 ± 0.25	-1.52 ± 0.17	-2.27 ± 0.16
U10445	-015 +047	$12800 \pm \frac{2230}{1280}$	8.00	8.05	7.96 ± 0.07	-1.17 ± 0.12	-0.72 ± 0.22	...	-2.22 ± 0.15
U10445	-010 +045	11200 ± 1500	8.10	8.17	8.10 ± 0.10	-1.33 ± 0.15	-2.26 ± 0.19
U10445	-003 +010	13900 ± 2000	7.90	8.11	7.90 ± 0.10	-1.06 ± 0.15	...	-1.42 ± 0.24	...
U11755	-003 +003	$11520 \pm \frac{290}{240}$	7.91	7.81	8.06 ± 0.03	-1.12 ± 0.06	-0.80 ± 0.07	-1.56 ± 0.07	-2.03 ± 0.07
U11755	-001 +000	$12400 \pm \frac{1380}{880}$	7.98	7.98	7.99 ± 0.05	-1.08 ± 0.09	-0.62 ± 0.16	-1.53 ± 0.12	-2.14 ± 0.11
U12713	-009 -003	13900 ± 2000	7.75	7.67	7.75 ± 0.10	-1.60 ± 0.15	-2.28 ± 0.18
U12713	-009 -003	13900 ± 2000	7.75	7.67	7.75 ± 0.10	-1.49 ± 0.16	-2.36 ± 0.21
U12713	-001 -003	$13780 \pm \frac{1680}{1120}$	7.84	7.79	7.80 ± 0.06	-1.54 ± 0.11	-0.81 ± 0.16	...	-2.23 ± 0.12
U12713	+004 +004	13200 ± 1500	7.75	7.80	7.75 ± 0.10	-1.50 ± 0.12

Table 6. Parameters of Additional Dwarf Irregular Galaxies

Galaxy	Distance [Mpc]	M_B	$(B-V)_0$	M_H/L_B	μ_B^0	$\log(M_{\text{dyn}})$	12 + $\log(O/H)$	$\log(N/O)$
Leo A	0.69	-11.52	0.26 ± 0.10	1.3	7.30 ± 0.05	-1.52 ± 0.15
GR 8	2.2	-12.12	0.38 ± 0.10	0.8	...	7.29	7.65 ± 0.06	-1.49 ± 0.07
UGC 9128	2.5	-12.63	0.25 ± 0.05	1.1	22.8	7.90	7.75 ± 0.05	-1.80 ± 0.12
UGC 2684	5.56	-13.03	0.34 ± 0.02	2.8	25.7	8.99	7.60 ± 0.10	-1.38 ± 0.07
UGC 8024	3.2	-13.33	...	7.3	...	9.42	7.67 ± 0.06	-1.68 ± 0.13
UGCA 20	8.65	-14.13	0.30 ± 0.01	2.6	24.2	9.34	7.60 ± 0.10	-1.56 ± 0.15
UGC 3174	7.86	-14.76	0.41 ± 0.02	2.2	23.4	9.48	7.80 ± 0.10	-1.56 ± 0.15
UGC 521	10.9	-15.17	0.30 ± 0.02	2.2	20.6	9.60	7.86 ± 0.04	-1.66 ± 0.12
UGC 5764	7.21	-15.3	...	0.7	...	8.99	7.95 ± 0.04	-1.34 ± 0.08
UGCA 357	16.5	-15.50	0.41 ± 0.01	3.4	25.2	9.91	8.05 ± 0.05	-1.55 ± 0.11
UGC 891	10.5	-15.53	0.46 ± 0.03	1.8	23.4	9.53	8.20 ± 0.10	-1.52 ± 0.13
UGC 5716	16.0	-15.53	0.42 ± 0.01	2.5	24.1	9.89	8.10 ± 0.10	-1.59 ± 0.10
UGC 300	19.8	-15.72	0.50 ± 0.01	1.4	23.3	...	7.80 ± 0.03	-1.50 ± 0.08
Haro 43	26.5	-16.31	0.41 ± 0.02	2.0	20.2	9.96	8.20 ± 0.10	-1.41 ± 0.10
UGC 5829	8.02	-16.6	...	1.3	...	9.89	8.30 ± 0.10	-1.76 ± 0.12
UGC 11820	17.9	-16.94	0.37 ± 0.02	2.1	23.7	10.17	8.00 ± 0.20	-1.59 ± 0.10
UGC 191	17.6	-17.52	0.46 ± 0.03	0.9	22.3	9.87	8.10 ± 0.05	-1.40 ± 0.10
UGC 634	31.4	-17.67	0.39 ± 0.03	2.0	23.1	9.98	8.18 ± 0.03	-1.58 ± 0.08
UGC 2984	20.6	-18.89	0.20 ± 0.02	0.5	20.5	9.99	8.30 ± 0.20	-1.57 ± 0.10

Note. — Distances are calculated from systemic velocities using a Virgocentric infall model and an H_0 of $75 \text{ km s}^{-1} \text{ Mpc}^{-1}$ except for Leo A (Dohm-Palmer et al. 1998), GR 8 (Dohm-Palmer et al. 1998), and UGC 9128 (Aparicio et al. 2000) which have TRGB distances in the literature. Colors, magnitudes, M_H/L_B , and oxygen and nitrogen abundances are from van Zee, Haynes, & Salzer (1997a,b) and van Zee, Skillman, & Haynes (2005).

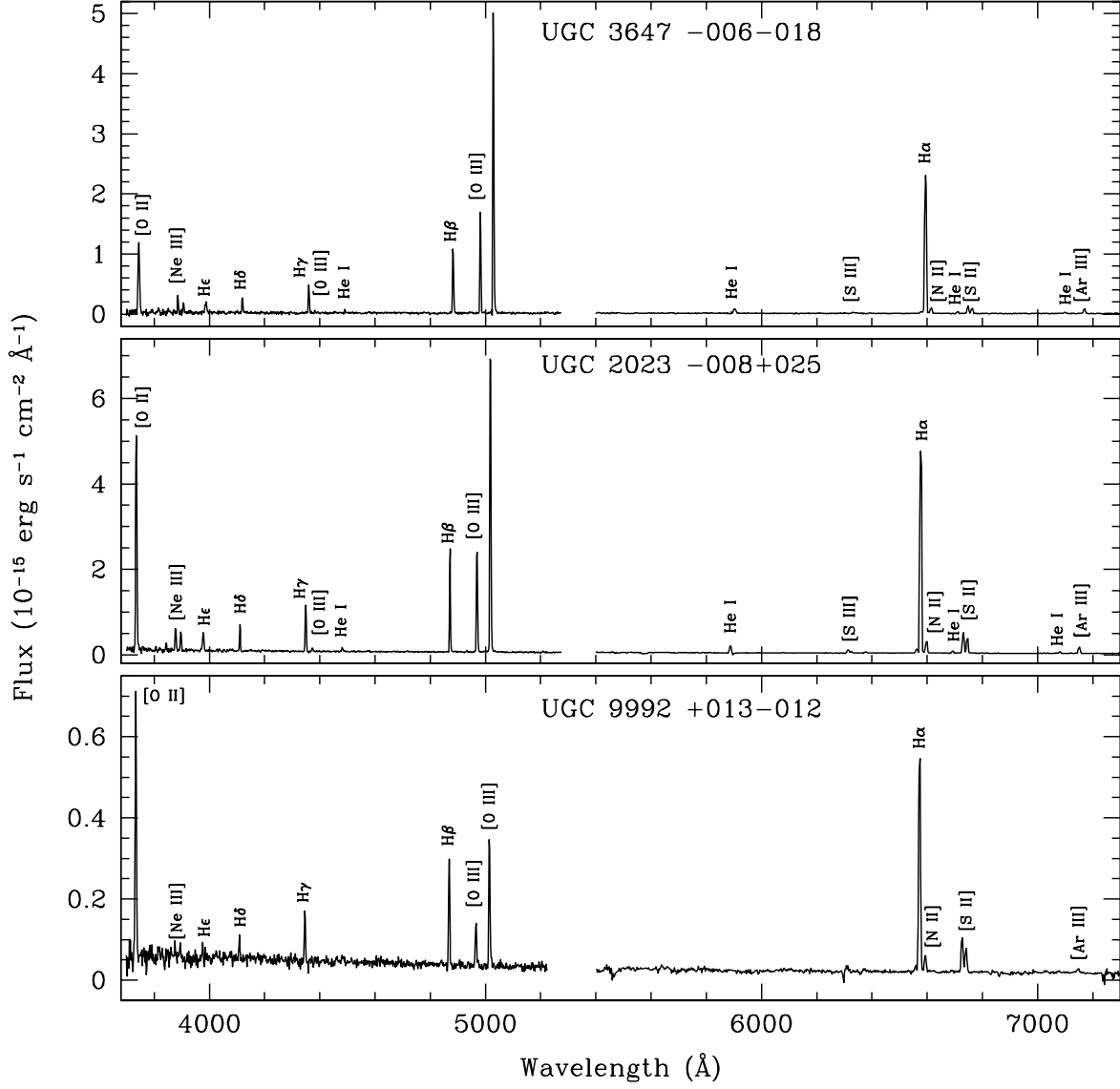


Fig. 1.— Representative optical spectra of H II regions in three low metallicity galaxies. All 3 H II regions shown here have similar oxygen abundances ($12 + \log(\text{O}/\text{H}) = 8.0$). However, the relative line strengths of [O II] and [O III] indicate that these 3 H II regions have very different ionization parameters. UGC 3647 -006-018 has one of the highest ionization parameters ($\bar{U} \sim 0.005$) in this sample, while UGC 2023 -008+025 is representative of the typical H II region in this sample ($\bar{U} \sim 0.002$) and UGC 9992 +013-012 has one of the lowest ionization parameters ($\bar{U} \sim 0.0006$).

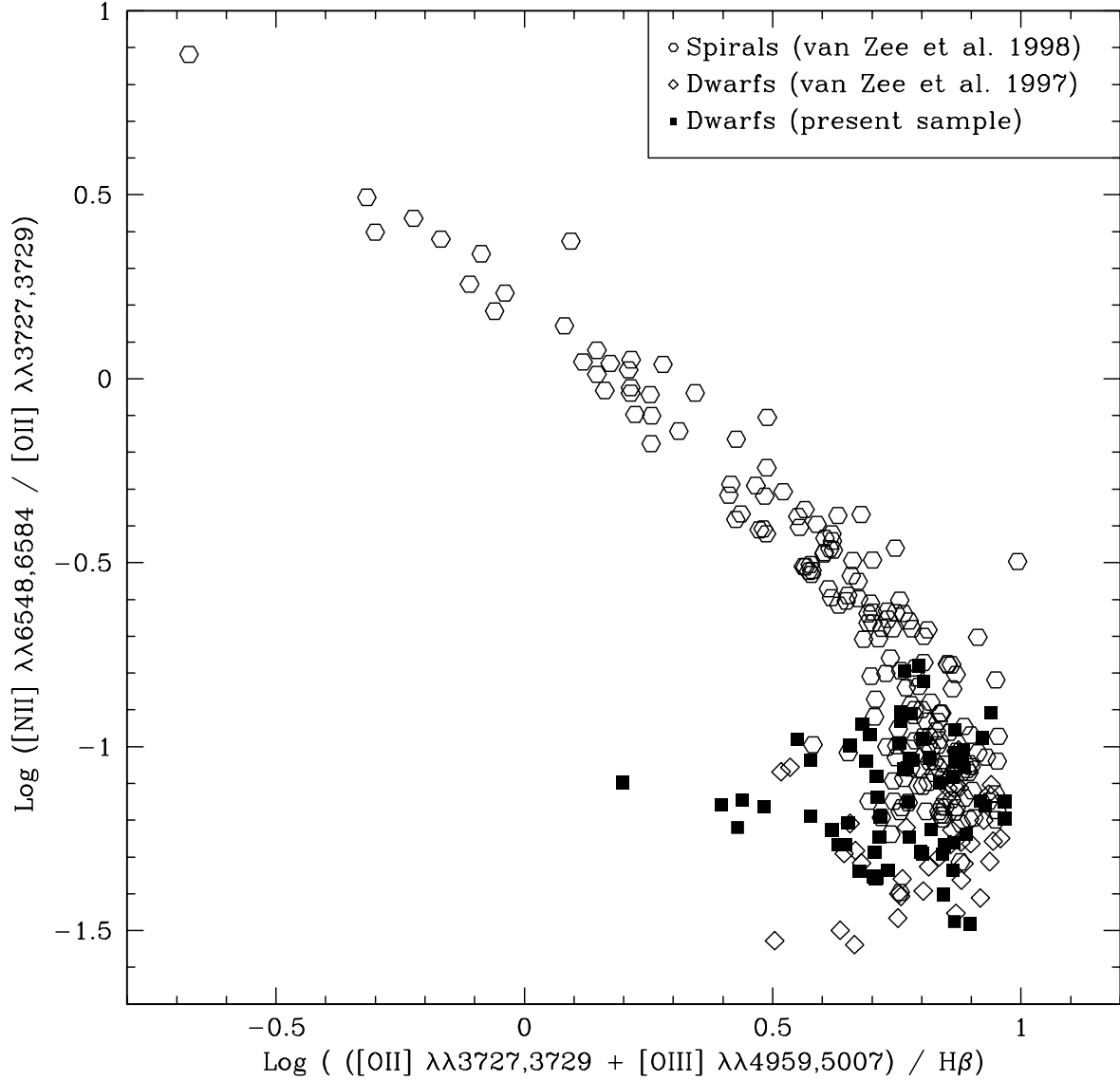


Fig. 2.— Diagnostic diagram for nitrogen and oxygen line ratios in dwarf irregular (present sample; van Zee et al. 1997) and spiral galaxies (van Zee et al. 1998). As expected, the low abundance HII regions in dwarf irregular galaxies have low $[\text{N II}]/[\text{O II}]$. However, the high metallicity H II regions in spiral galaxies trace a fairly narrow locus in this diagram while the low abundance H II regions in dwarf irregular galaxies exhibit a wide range of $[\text{N II}]/[\text{O II}]$ for a given value of R_{23} .

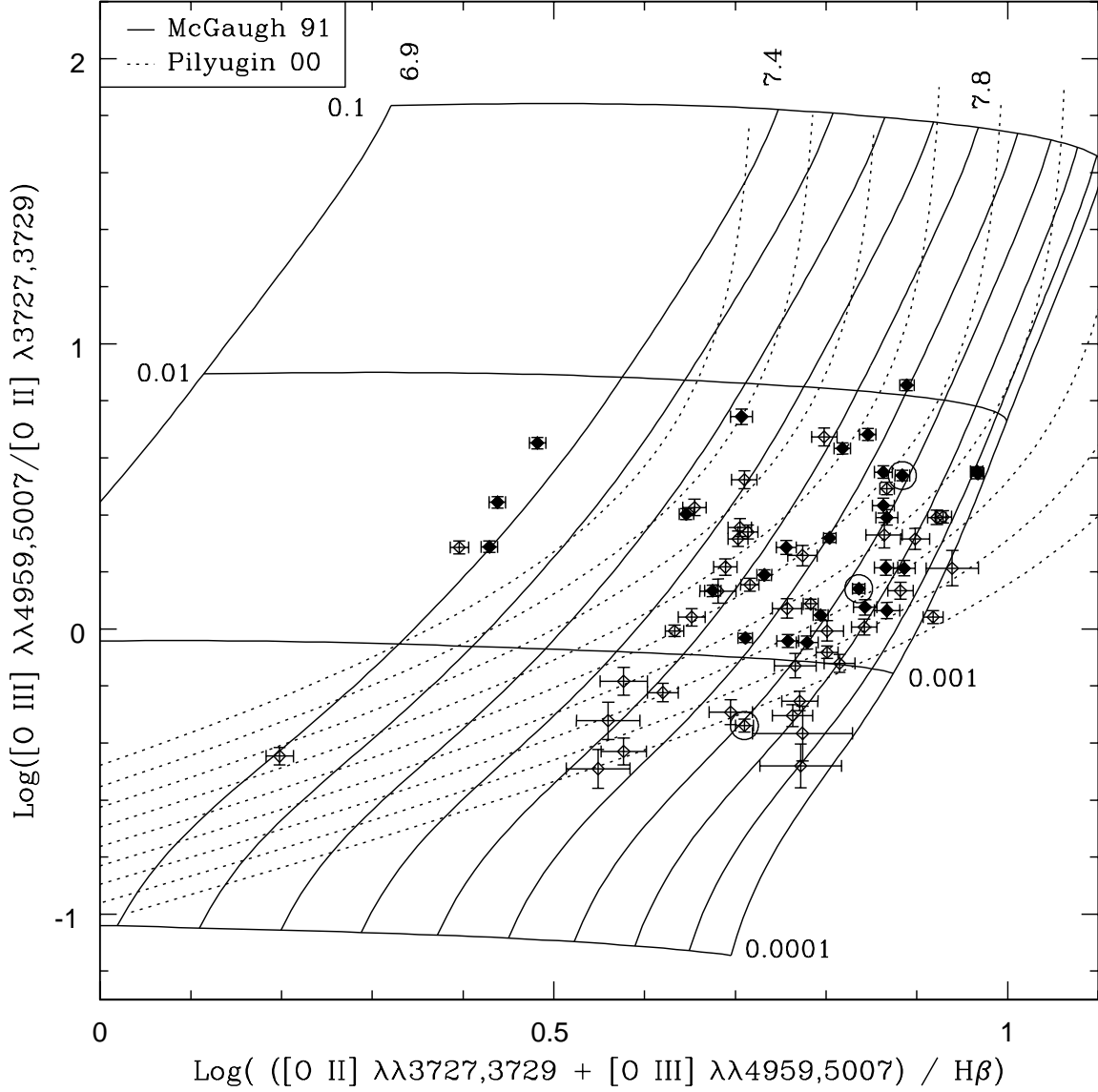


Fig. 3.— Model grid of the lower branch of the R_{23} relation from McGaugh (1991) (solid lines). Also shown are the empirical metallicity calibration relations derived by Pilyugin (2000) for $7.4 < 12 + \log(\text{O}/\text{H}) < 8.2$ (dashed lines). The locations of H II regions in this sample are marked; filled diamonds represent H II regions with solid detections of $[\text{O III}] \lambda 4363$. The circled points correspond to the representative H II regions shown in Figure 1. The five extremely low metallicity points ($12 + \log(\text{O}/\text{H}) \sim 7.35$) are all observations of H II regions in UGCA 292.

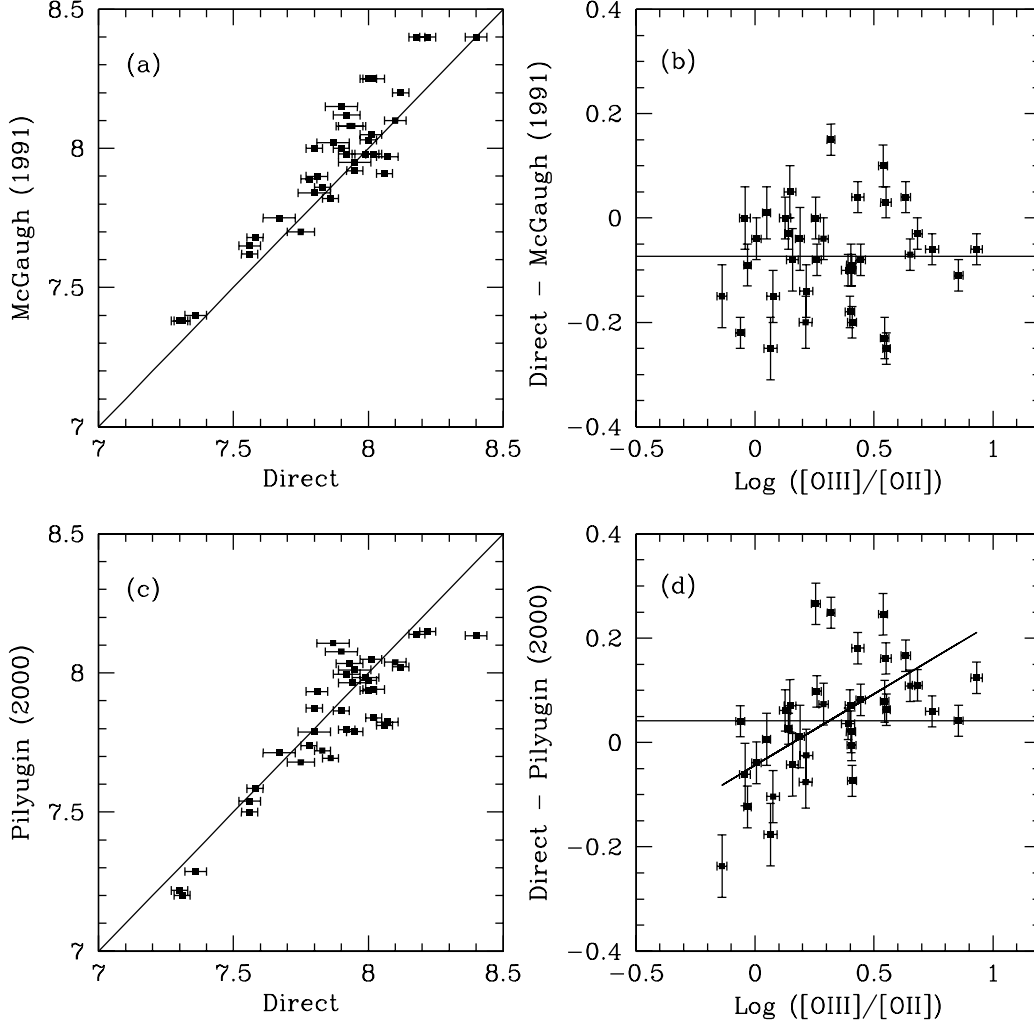


Fig. 4.— Comparison of empirical and direct abundance calibrations for H II regions in dwarf irregular galaxies with detected [O III] $\lambda 4363$ emission. The plots include H II regions in the present sample as well as observations reported in van Zee et al. (1997). Both the McGaugh (1991) and Pilyugin (2000) calibrations have systematic offsets from the direct oxygen abundance calculation. (top panels) The photoionization models from McGaugh (1991) appear to overpredict the oxygen abundance by 0.07 dex. (bottom panels) The p-method (Pilyugin 2000) appears to underpredict the oxygen abundance by ~ 0.04 dex, but there is a systematic correlation with the ionization parameter in the sense that the p-method significantly (0.1 - 0.2 dex) overpredicts the oxygen abundance for low excitation H II regions.

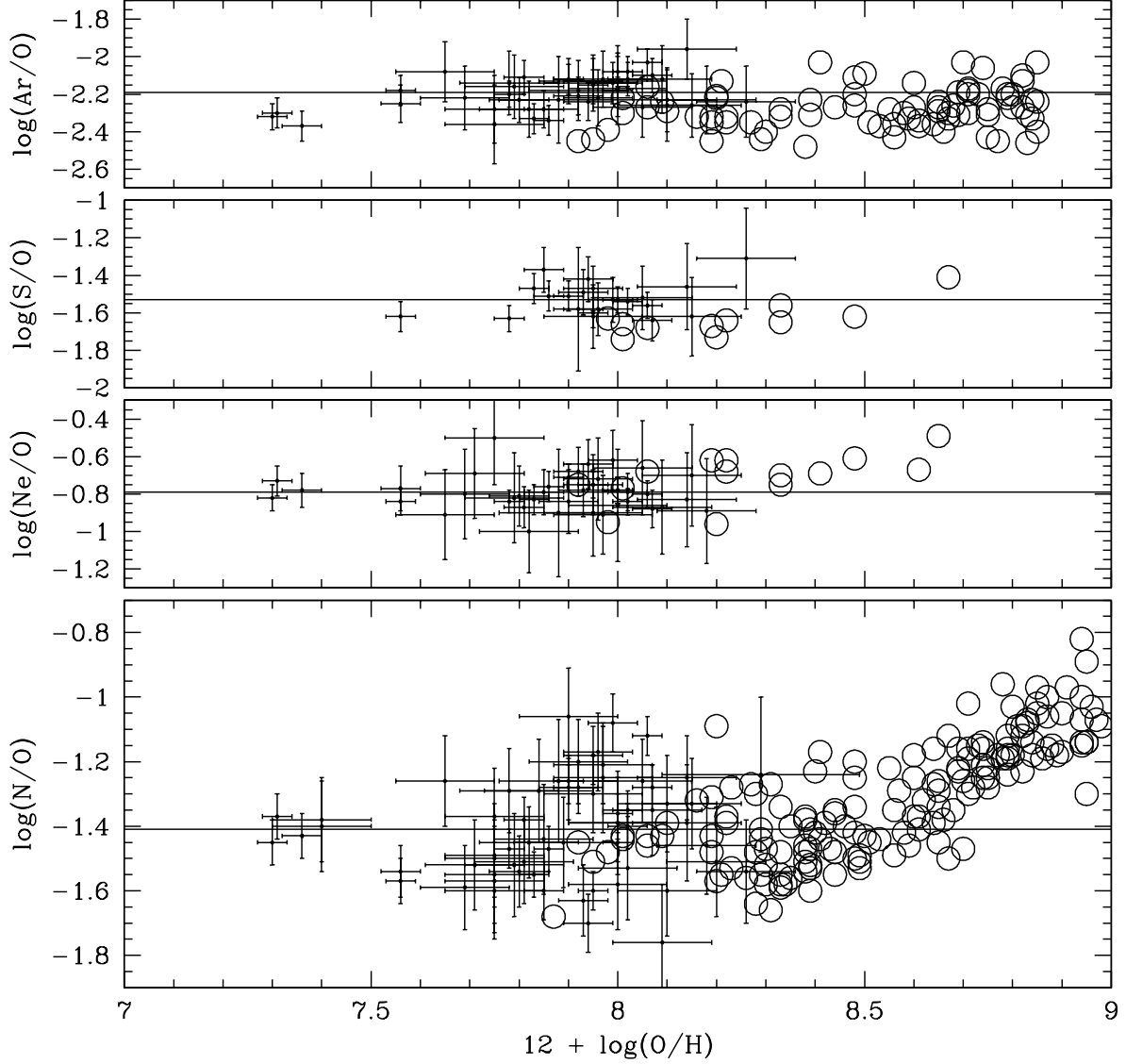


Fig. 5.— H II region elemental abundances for nitrogen, neon, sulfur, and argon as a function of oxygen abundance. The figures include H II regions of dwarf irregular galaxies from the present sample as well as observations reported in van Zee et al. (1997); open circles denote H II regions in spiral galaxies (van Zee et al. 1998). As expected, the alpha elements (neon, sulfur, and argon) show no trend with increasing oxygen abundance, while the N/O ratio is approximately constant at low abundances (primary nitrogen), but then increases as the oxygen abundance increases (secondary nitrogen).

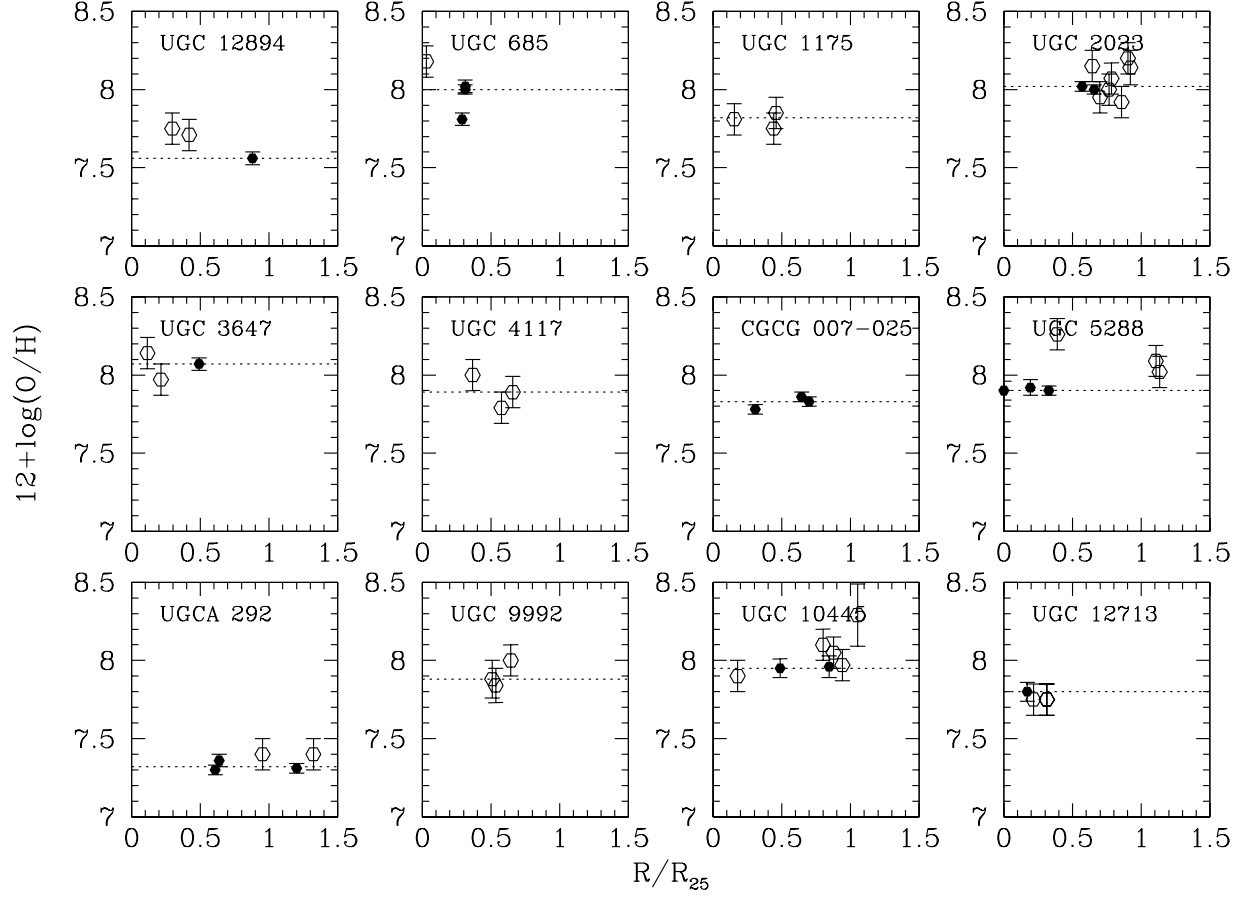


Fig. 6.— H II region abundances as a function of (normalized) galactic radius; filled symbols represent H II regions with solid detections of $[O\ III] \lambda 4363$. In most instances, the H II region abundances are similar at all radii. Note that the apparent trend in UGC 12894 may be a result of an overestimate of the inner H II region oxygen abundances (strong line method). The dashed line indicates the mean metallicity listed in Table 1.

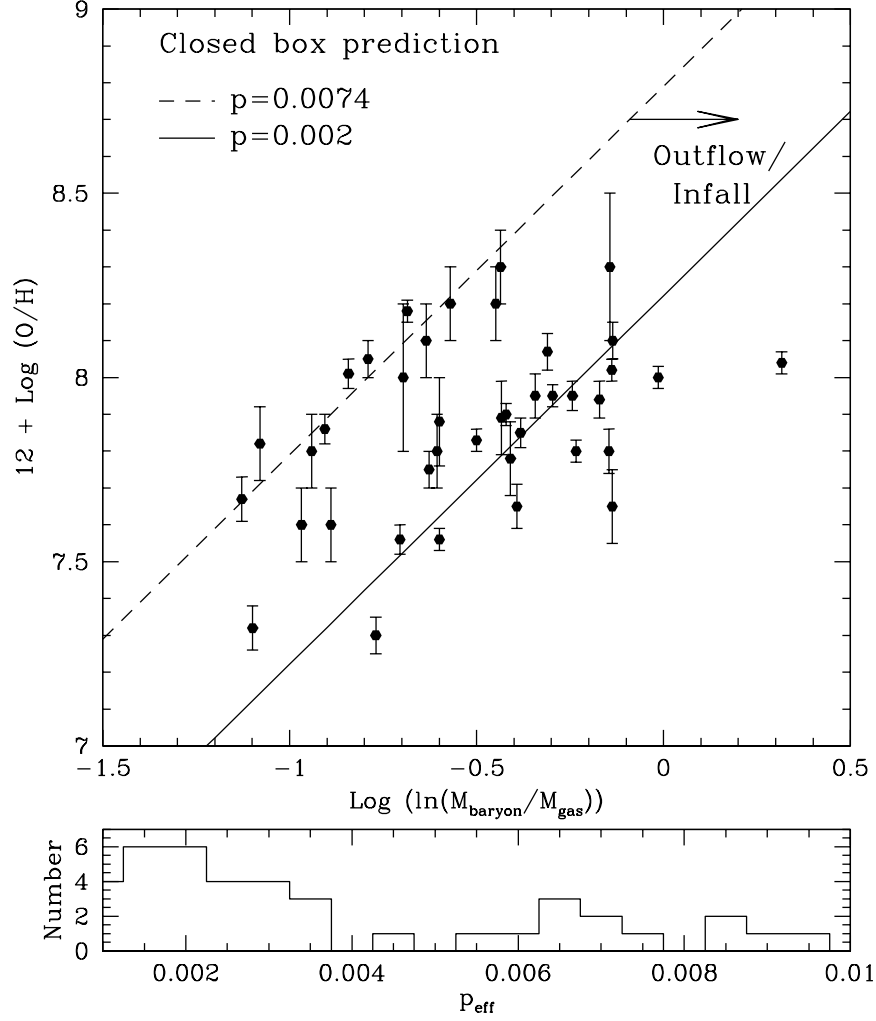


Fig. 7.— Comparison of the observed oxygen abundance and that predicted by simple closed box chemical evolution models with instantaneous recycling and constant star formation rates. The dashed line indicates the expected one-to-one trend if dwarf irregular galaxies are closed boxes with an oxygen yield appropriate for low metallicity galaxies with a Salpeter IMF ($p = 0.0074$, Meynet & Maeder 2002). The solid line indicates the expected one-to-one trend if dwarf irregular galaxies evolve as open boxes with an effective yield $\sim 1/4$ of the true yield. The bottom panel shows the histogram of effective yields for this sample of dwarf galaxies. While the majority of dIs appear to evolve as open boxes (due to either infall of pristine gas or outflow of enriched material), several of the dwarf irregular galaxies in this sample appear to be consistent with closed box chemical evolution.

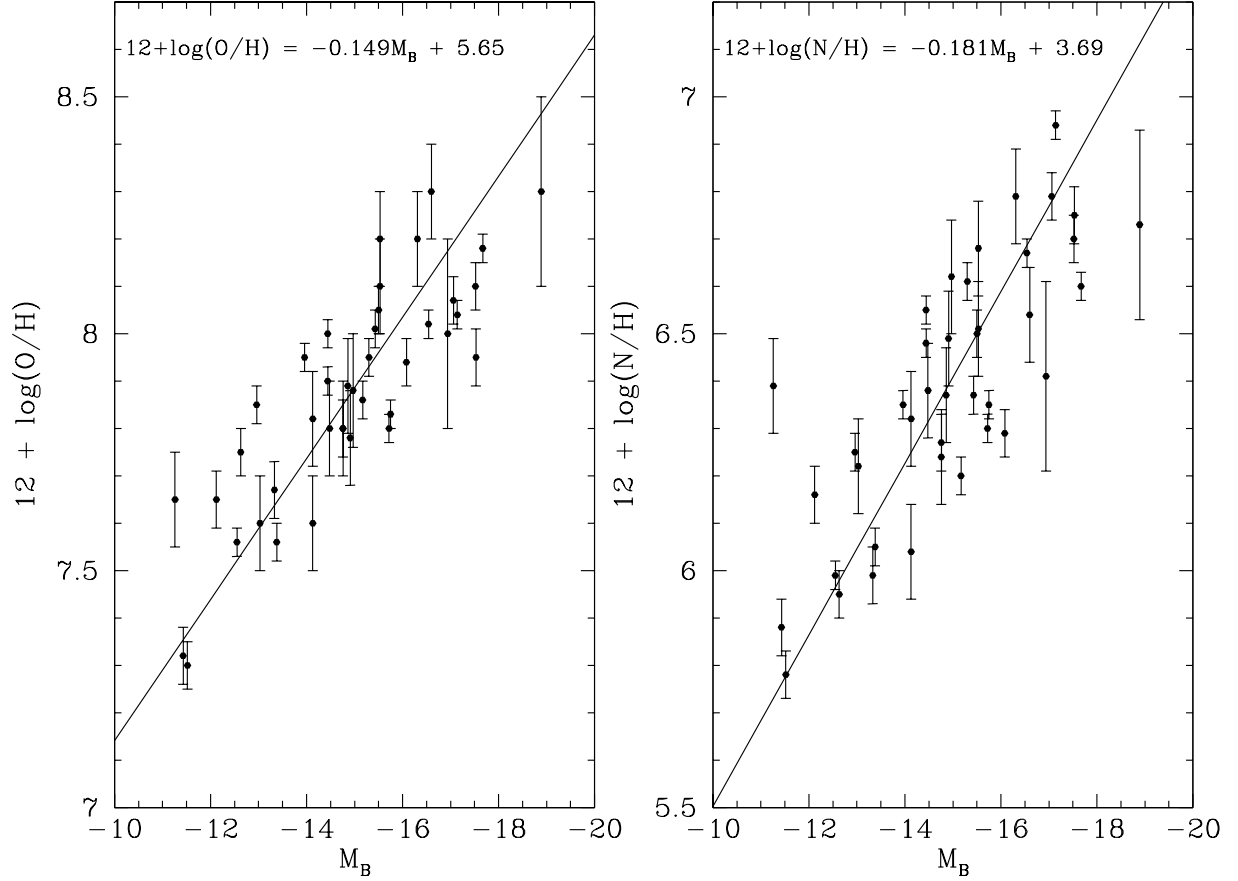


Fig. 8.— Metallicity-luminosity relationships for isolated dwarf irregular galaxies (present sample; van Zee et al. 1997; van Zee et al. 2005). Correlations between luminosity and both oxygen and nitrogen abundances are shown.

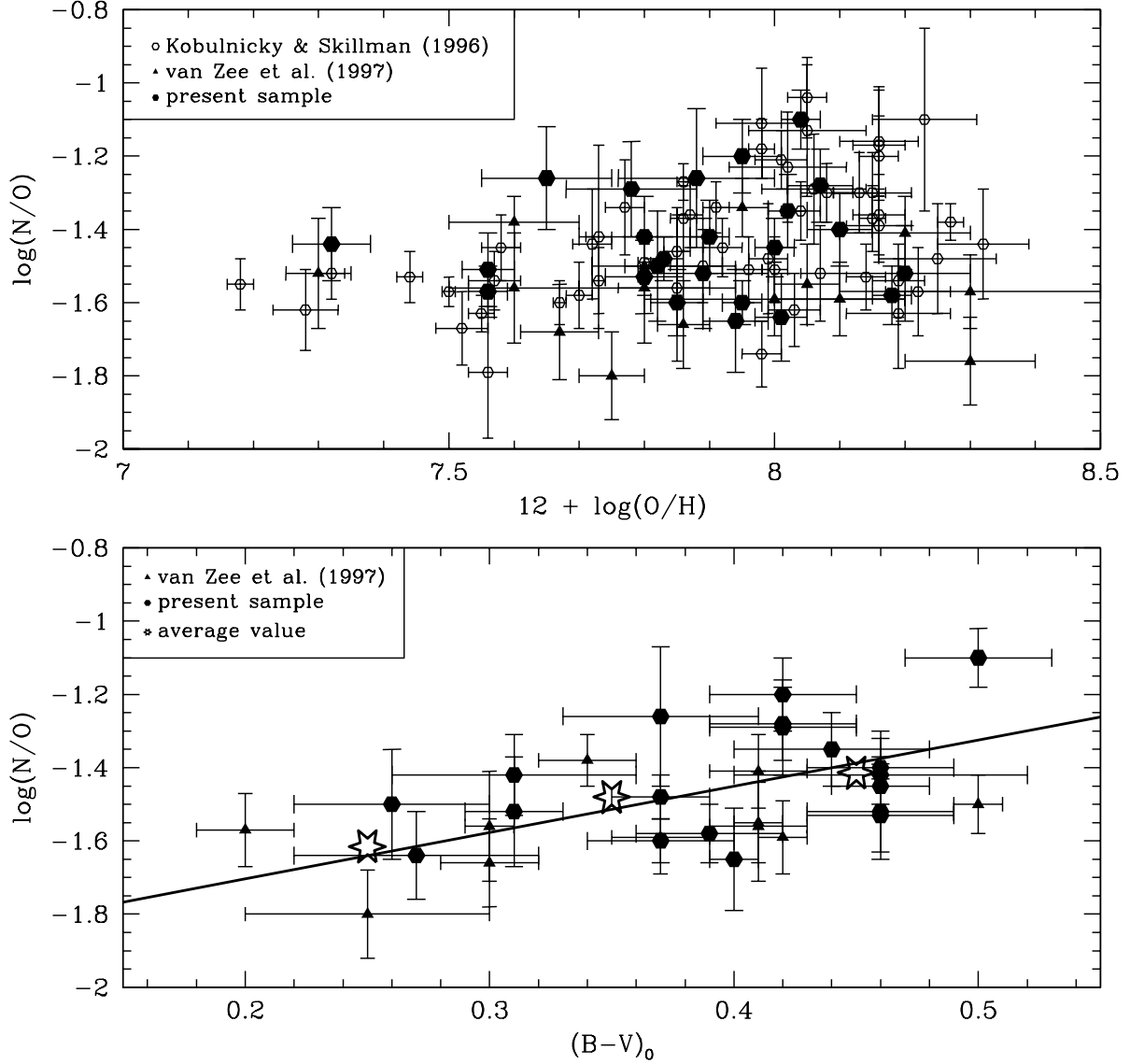


Fig. 9.— (Top) Global nitrogen and oxygen abundances for dwarf irregular galaxies. The filled symbols are from the present (hexagons) and previous (triangles; van Zee et al. 1997; 2005) studies of dwarf irregular galaxies. The open symbols are from the literature compilation by Kobulnicky & Skillman (1996); only galaxies without WR emission features have been plotted. (bottom) Correlation between nitrogen-to-oxygen ratio and color of the underlying stellar population. Redder galaxies have higher N/O ratios as would be expected for a time delay between the release of oxygen and nitrogen.

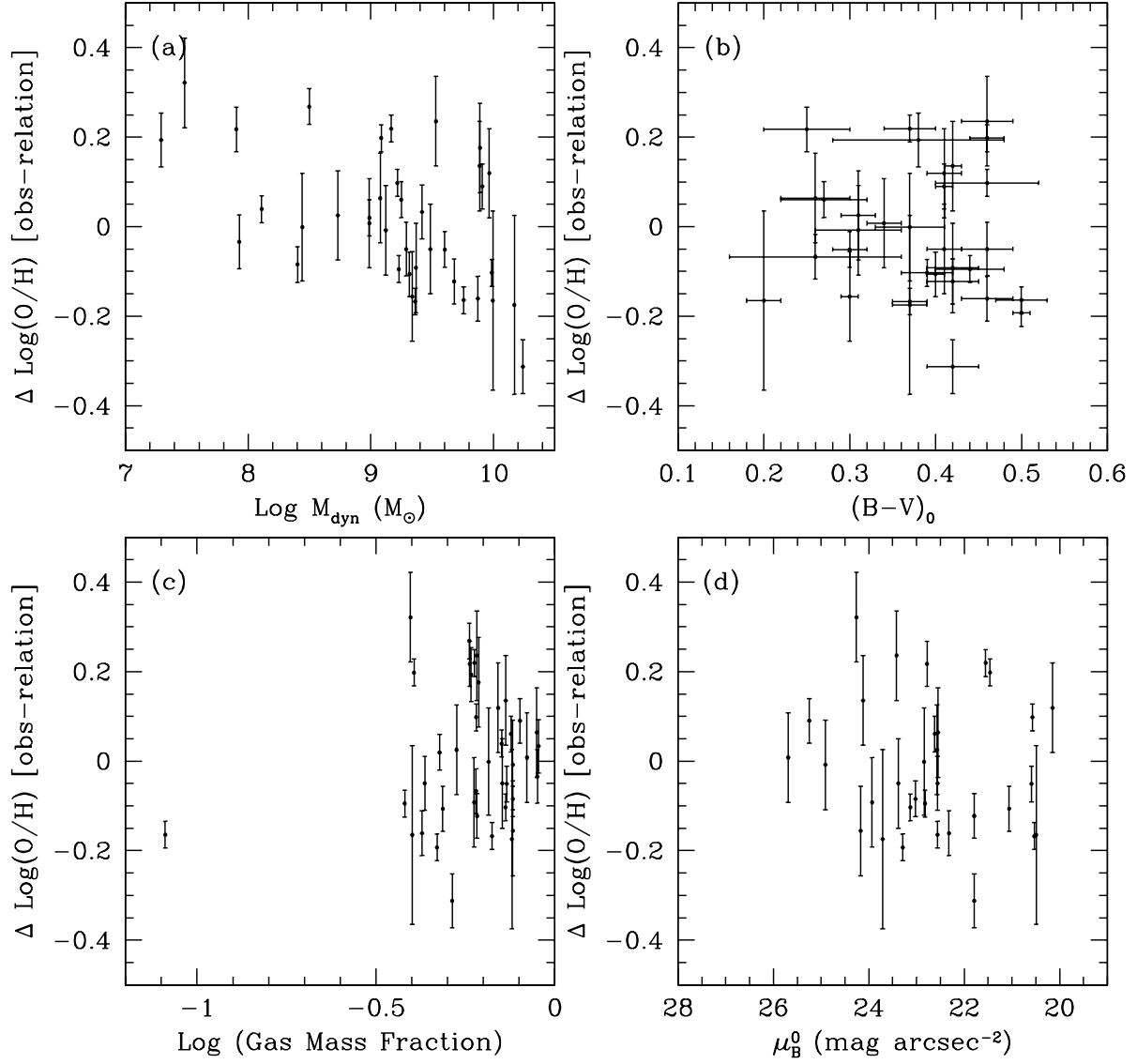


Fig. 10.— Residuals in the metallicity-luminosity relation plotted as a function of other global galaxy parameters: (a) dynamical mass, (b) color of the underlying stellar population, (c) gas mass fraction, and (d) central surface brightness.

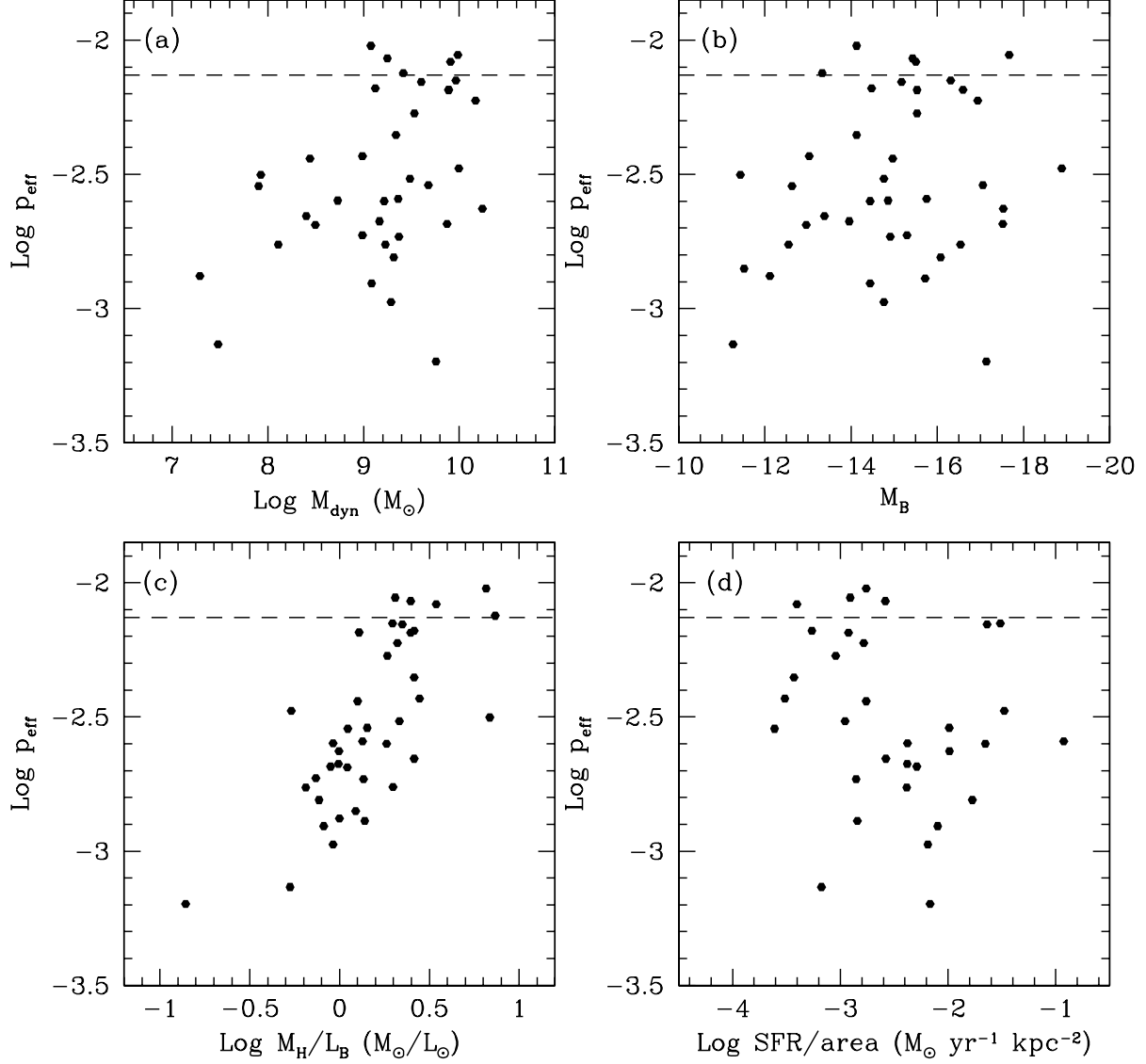


Fig. 11.— The effective yield plotted as a function of global galaxy parameters: (a) dynamical mass, (b) absolute blue magnitude, (c) gas richness (M_H/L_B), and (d) surface star formation rate (star formation rate/area). The closed box yield is denoted by the dashed line in each plot. The effective yield correlates strongly with gas richness, but no other global trends are evident.